

Atomistic investigation of cavitation and ablation in tantalum foils under irradiation with x-rays approaching 5 keV

M. J. Duff^{1,*}, P. G. Heighway², J. D. McHardy¹, A. D'Souza², R. S. McWilliams¹, J. S. Wark², and M. I. McMahon¹

¹*School of Physics and Astronomy, Center for Science at Extreme Conditions, and SUPA, University of Edinburgh, Peter Guthrie Tait Road, Edinburgh EH9 3FD, United Kingdom*

²*Department of Physics, Clarendon Laboratory, University of Oxford, Parks Road, Oxford OX1 3PU, United Kingdom*



(Received 15 October 2021; revised 27 May 2022; accepted 17 June 2022; published 11 July 2022)

The rapid irradiation and heating of matter can lead to material removal via a process known as ablation. While previous investigations have focused on ablation with optical and soft x-ray pulses, the process is not well understood for the high-energy x-rays delivered at current x-ray free electron laser facilities. In this paper, we use hybrid two-temperature model molecular dynamics simulations to determine the damage threshold and dynamics for tantalum foils under irradiation with x-rays in the range 1–5 keV. We report that damage occurs for foils with thickness ≥ 300 nm when heated to around 1.25 eV/atom. This damage results from the combined processes of melting and cavitation, finally resulting in the removal of material layers. The predictions of this study, in terms of the cavitation threshold and underlying dynamics, could guide interpretation of experiments as well as applications including development of beamline optics for free-electron lasers. We report consistency between cavitation and ablation behavior in isochoric heating experiments and spall processes in hydrodynamic compression and release experiments, confirming the primary modes of damage are mechanical in nature for the x-ray energies investigated.

DOI: [10.1103/PhysRevB.106.024107](https://doi.org/10.1103/PhysRevB.106.024107)

I. INTRODUCTION

Irradiation of materials by short pulses of energetic radiation leads to the removal of layers of matter, and localized destruction, via a process known as ablation. This is a process of interest to industry due to its capability to imprint microstructures on surfaces [1–4] as well as the potential to improve beamline optics through a deeper understanding of the mechanisms by which damage occurs under intense irradiation. The minimum fluence at which damage occurs in a material is the ablation threshold, the measurement of which can provide information on material properties as well as on the parameters of the incident radiation. For example, extensive work has been conducted in Refs. [5–10] into the use of the ablation profile imprinted on materials by XUV and hard x-ray pulses to diagnose the spatial characteristics and transverse intensity profile of the incident beam. Numerous experimental studies have reported on the ablation threshold for a range of metals under irradiation spanning a wide range of wavelengths and pulse durations [1,11–14]. Despite these efforts, there remain gaps in the theoretical understanding of the ablation process, particularly under hard x-ray irradiation.

The dynamics of the x-ray matter interaction are strongly dependent on the properties of the material and the characteristics of the incident irradiation. There are, however, general features of the irradiation and subsequent ablation processes, which will be briefly outlined. The incident x-ray photons are scattered or absorbed, depending on the x-ray energy and

the atomic number of the material. For transition metals such as tantalum, interacting with ≈ 10 keV photons, absorption is the dominant process. The x-rays interact with the inner shell electrons, resulting in liberation of photoelectrons, fluorescence, or the emission of Auger electrons (which are more important in low- Z elements). These processes result in rapid redistribution of the electron energy, and equilibration of the free electron gas over a timescale of ≈ 100 femtoseconds (fs). In the case of very short pulses of intense radiation [for example, the ≈ 100 fs pulses deliverable by x-ray free electron lasers (XFEL)], the electrons reach extremely high energy densities following irradiation. The transfer of heat from the electrons to the lattice occurs over a much longer timescale, of the order 10 s of picoseconds (ps). This rapid heating of the lattice occurs faster than the timescale associated with thermal expansion, which is determined by the speed of sound (typically in the range 10–100 ps). Heating therefore occurs under isochoric conditions, resulting in the formation of a large thermal pressure within the material. This isochoric heating can also occur in materials irradiated with optical and UV radiation [15–17]. Specifically, during hard x-ray irradiation, there is the complication that the emitted photoelectrons change the internal charge distribution. This can lead to Coulomb forces playing an important role in the ablation process, and the resulting damage dynamics are not well understood [16].

Following the isochoric heating stage, the thermal pressure within the sample is released over the timescale of thermal expansion. The dynamics of the pressure release depend on the uniformity of the heating. Existing studies have reported on the conditions under which metals undergo

*Corresponding author: mduff@ed.ac.uk

ablation following irradiation with optical and soft x-ray pulses [1,18–24]. Due to the short penetration depth of such radiation, only a small volume near the surface of the metal is heated. The resulting localized thermal pressure is released by launching a leading (compressive) wave into the bulk of the material, accompanied by a trailing (rarefaction) wave propagating from the front surface as it expands into vacuum. The superimposed wave has a bipolar spatial profile and propagates toward the rear surface. This wave is subsequently reflected, with the leading component transitioning into a tensile one and overlapping with the incoming trailing wave to form a region of tension within the metal [19,25]. For a sufficiently high degree of heating (and therefore release of a large thermal pressure), the tensile stress may exceed the tensile strength of the material. Note that this situation, where the release of pressure drives a bipolar wave into the material, is analogous to the seminal work by Thomsen [26], who derived the equations governing the propagation of waves in a weakly anisotropic medium.

In contrast, if the entire metal is uniformly heated (and there is no pressure gradient), the pressure waves do not exhibit the bipolar spatial profile described previously. Instead, rarefaction waves are released from the upstream and downstream free surfaces simultaneously as they expand into vacuum. This uniform heating can occur even when the initially heated volume is small if the material has a large thermal conductivity or if heat is carried deep into the bulk by highly energetic electrons.

Thus, for materials subjected to hard x-ray irradiation, the uniformity of the heating falls between the two extremes described above. From the experimental perspective, the thickness of material is often chosen to be approximately equal to the absorption depth of the incident radiation, *i.e.*, the distance over which the electron temperature decreases to $1/e$ of the surface value. This condition is a compromise between having a sufficiently thick sample that there is a strong scattering signal without being too thick that both the incident and scattered x-rays are absorbed, resulting in a decrease in signal at the sample rear. This condition results in a pressure and temperature gradient across a greater extent of the material compared to the case for weakly penetrating radiation. The propagation of the pressure waves from the free surfaces is further complicated by the fact that the temperature gradient in the sample means different regions have different tensile strength limits. This can lead to localized ablation [27], which does not necessarily occur at the center of the material as it does for uniform heating.

The formation and decomposition of a stress-confined state under intense heating via pulsed radiation exposes the complexity of the ablation dynamics. While experiments are only partly sensitive to these dynamics, hybrid two-temperature model molecular dynamics (TTM-MD) simulations can explore them in detail [28,29]. In contrast to standard MD, the TTM-MD approach enables energy to be coupled to an electron subsystem and slowly transferred to the lattice. The unique advantage offered by this approach is that, unlike finite-difference and hydrodynamic simulations, it is possible to track individual atomic trajectories throughout the interaction. This is particularly important for high energy ablation processes. The applicability of the TTM-MD approach has

been demonstrated in recent computational studies, where the predictions of the ablation threshold and crater depth show agreement with experimental measurements [19,21].

A limitation of the aforementioned studies is that they are restricted to the regime of weakly penetrating radiation [1,18–24]. We aim to extend the simulation approach to incorporate higher energy x-rays, in the range 1–5 keV, where the ablation process is poorly understood. This energy is within the operating range of current XFEL facilities and provides a means of interpreting recent experimental results. While previous studies have investigated the pressure-induced phase transitions [30] and tensile strength of tantalum using simulations of shock compression and release [27,31–33], here we specifically simulate the isochoric heating and subsequent pressure release which leads to material failure.

This paper presents numerical simulation results which explore the cavitation threshold and subsequent ablation dynamics for tantalum foils under intense x-ray irradiation (up to ≈ 5 keV). In Sec. II, an overview is provided of the different mechanisms by which ablation occurs under short pulse irradiation. This is followed in Sec. III by a discussion of the TTM-MD approach implemented in the open-source molecular dynamics code, LAMMPS [34], employed in this study. The key results, namely, the criteria for destruction of foils of different thickness values, are presented in Sec. IV. Finally, the results are summarized in Sec. V along with a discussion of their wider impact and relevance to XFEL experiments.

II. UNDERPINNING THEORY

A. Ablation mechanisms under femtosecond pulse irradiation

There are numerous mechanisms which can result in the destruction of material under pulsed radiation. The exact mechanism which dominates an interaction depends on the duration of the radiation pulse, as well as material properties including the speed of sound, thermal conductivity, and, in the case of metals, the rate of energy transfer from the electron subsystem to the lattice. A complete understanding of the process of material removal (ablation) is further complicated by the fact that the mechanisms can feed into each other, operating in different regions of the material on the same timescale [35]. In this section, a brief overview is provided of the ablation mechanisms present in materials under ultrashort pulse irradiation.

As discussed in the Introduction, femtosecond pulse irradiation results in the formation and decomposition of a stress-confined state. Subsequent pressure release creates tension, which can lead to failure of the material if the tensile strength is exceeded. Otherwise, the pressure waves continue to reverberate within the sample and can, for example, be used to generate off-Hugoniot states in layered samples [36]. If the material remains solid up to the point of failure, this process is known as spallation. The phase diagram for tantalum is plotted in Fig. 1, where the black curve labeled (1) indicates a typical thermodynamic trajectory associated with spallation as described in Refs. [37,38]. The process begins with isochoric heating, indicated by the vertical section of the trajectory. This heating is insufficient for melting, and the trajectory

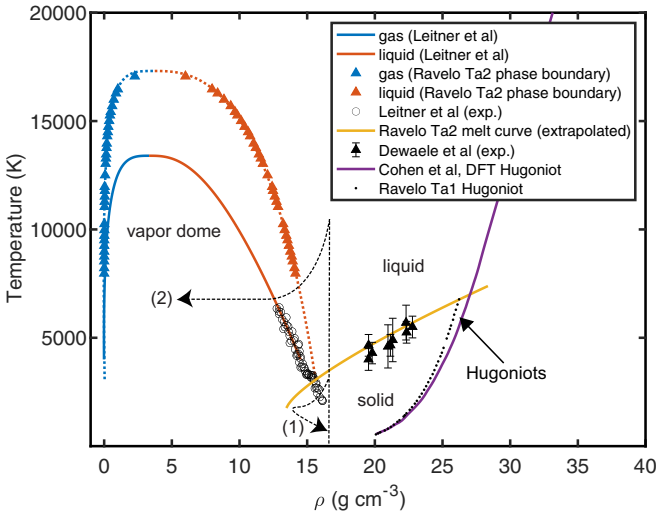


FIG. 1. Tantalum phase diagram. The solid blue and orange curves indicate the vapor dome boundaries obtained from Ref. [48]. These boundaries are extrapolated from the experimental data points marked by open circles at the liquid end of the phase boundary. The blue and orange triangles mark the vapor dome boundaries (i.e., the binodal line) obtained from mixed phase simulations (described in the Appendix) using the Ravelo Ta2 potential from Ref. [31]. The dotted blue and orange curves are fitted to the mixed phase simulation data points, using the same fitting equation as Ref. [48]. The yellow curve is the melt curve for the Ravelo Ta2 potential used in this paper, with black triangles indicating the experimental data points from Ref. [49] used in the fitting of this EAM potential. The melt curve is extrapolated to negative pressure values using the fitting equation presented in Ref. [50] and converted to density-temperature space using the Equation of state (EOS) spreadsheet in Ref. [51]. The Hugoniot (purple curve) is obtained from Density functional theory (DFT) calculations in Ref. [52] while the dotted black curve is the Hugoniot calculated using the Ravelo Ta1 potential in Ref. [31]. The vertical dashed line is the ambient density isochore for tantalum, with branches (1) and (2) representing thermodynamic pathways associated with spallation and cavitation, adapted from Ref. [37].

is subsequently constrained to the solid region of the phase diagram.

The high levels of lattice heating achievable under femtosecond irradiation mean that the material is often heated above its melting point. Analogously to the process of spallation in solids, liquid metals can undergo failure when they are subjected to tensile stress which exceeds their tensile strength. This process is known as cavitation. It resembles boiling in that it proceeds through the formation of voids or cavities in the material, but at temperatures below the boiling point [25,39]. The process of cavitation is possible due to tensile stresses within the liquid, which drive the void formation.

The thermodynamic trajectory for cavitation is plotted in Fig. 1 and denoted by the curve labeled (2). Following the initial isochoric heating stage, the sample undergoes isentropic cooling and crosses into the vapor dome between the triple and critical points. The material then exists as a metastable liquid, which will eventually transition into a mixed liquid-vapor phase if an energy barrier is overcome [40,41]. This barrier is that the pressure in the vapor phase must exceed

the pressure in the liquid plus the pressure associated with the surface tension across the interface separating the phases [42]. This is written in Eq. (1) below:

$$P_v > P_l + \frac{2\sigma}{r}. \quad (1)$$

In the above equation, σ is the surface tension measured in units of Jm^{-2} and r is the radius of the void. Equation (1) suggests there is a critical radius where the probability of the forward and backward phase transitions are equally likely [41]. This critical radius has been evaluated for Cu to be 3–4 Å in Ref. [43] and 7.3 Å in Ref. [41], using a combination of classical nucleation theory and MD simulations. We do the same for tantalum in the Appendix, yielding a value of 4.2 Å. While this radius denotes the size at which the void is likely to continue growing, there is still a probability that a critically sized void will collapse at later times [41]. This is especially relevant in a system where reverberating pressure waves can disrupt the equality in Eq. (1), which is the case for the foils in this study.

The process of normal boiling is not possible on the timescale of a femtosecond pulse, as noted in Ref. [44]. Instead, the process of phase explosion (or explosive boiling) becomes dominant. In this case, a layer of material near the irradiated surface is heated to its stability limit, typically understood to occur at $0.9T_c$ where T_c is the temperature at the critical point [35]. The material exists as a superheated liquid, i.e., it remains in the liquid state but is heated above the boiling point, and phase explosion is the rapid phase transition from this superheated liquid to a two-state mixture of liquid and vapor [35]. There are a number of signatures which characterize the phase explosion process, including a sharp increase in the yield of ablated atoms [45], a change in the ablated plume from distinct liquid layers to a mixture of vapor-phase atoms and clusters [35,37,38], and a high nucleation rate as the trajectory approaches the spinodal line (the stability limit) [37].

In this paper, we follow the thermodynamic trajectory of sections of the foil (which are representative of the average bulk material) through phase space to diagnose the ablation mechanism. This approach is outlined in Refs. [37,38,46,47]. We note that Refs. [37,38] are limited by the use of 2D simulation geometry and make incorrect predictions about the conditions for phase explosion. Here we use fully 3D simulations and limit our discussion to lower energy mechanisms (spallation and cavitation), which can be reasonably inferred by investigating whether or not the trajectory crosses the melt curve and subsequently progresses into the vapor dome (measured for the chosen MD potential). We do not typically consider phase explosion given that the level of heating is well below the critical temperature, even close to the upstream free surface where the temperatures are highest.

III. METHODOLOGY

A. Computational model

In this investigation, we employ hybrid TTM-MD simulations, performed with the open-source code LAMMPS

[34]. The development of the TTM module for LAMMPS is detailed in Refs. [53,54] and the underlying algorithm is described in Refs. [28,29]. In these TTM-MD simulations, the atomic lattice is overlaid with a grid of electron cells. The radiation energy is deposited into the grid, with the temporal evolution of the grid temperature determined by solving the heat conduction equation, shown below, using a finite difference scheme:

$$c_e \rho_e \frac{\partial T_e}{\partial t} = \nabla \cdot (\kappa_e \nabla T_e) - G(T_e - T_a) + \frac{I_0}{\ell_s} \exp\left(-\frac{x}{\ell_s}\right). \quad (2)$$

In the above equation c_e is the electron heat capacity and κ_e is the electron thermal conductivity. It is important to note that, in LAMMPS, it is possible to incorporate the dependence of both c_e and κ_e on the electron temperature. The electron temperature and density are denoted T_e and ρ_e respectively, while T_a is the atomic (lattice) temperature. The rate of heat transfer from the electrons to the atoms is determined by the electron-phonon coupling constant, G , which has been calculated for a range of materials and as a function of electron temperature in Refs. [[55–57], and measured specifically for tantalum in Ref. [58]. The final term on the right of Eq. (2) is the radiation source term [23]. The absorbed intensity is denoted I_0 and the term ℓ_s is the absorption depth. The energy is only deposited into electron cells with nonzero temperature, i.e., there is no energy exchange with the vacuum regions. As the foil expands into vacuum, the electron cells in the regions which were previously unoccupied by atoms obtain a nonzero temperature. This subsequently enables heat exchange with neighboring (nonvacuum) cells. The values of all the above parameters used in this paper are detailed in the next section.

The electron cells act as finite heat reservoirs for the atoms located in the same volume. Heat is passed from the electrons to the atoms via a Langevin thermostat. The equation of motion for a given atom (with mass, m_a , and velocity, v_a) is given in Eq. (3) below:

$$m_a \frac{\partial v_a}{\partial t} = F_a(t) + \tilde{F}(t). \quad (3)$$

The first term on the right is the force exerted on the atom due to the interatomic potential, while the second term is a force associated with the Langevin thermostat. The electron cell acts as a finite heat reservoir, giving kicks to the trajectory of atoms located within the same volume, with an amplitude proportional to the temperature of the local electron cell. This interaction simulates the electron-phonon coupling which is responsible for energy transfer from the electron subsystem to the atomic lattice.

Following the method prescribed in Ref. [53], the TTM module runs until the temperatures of the electron subsystem and the lattice reach equilibrium (when the average electron and lattice temperatures in the foil are within 100 K of each other), at a time denoted τ_{eq} . This time depends on the energy deposited into the electron subsystem, with τ_{eq} increasing with the deposited energy. For the range of deposited energy under investigation, τ_{eq} occurs before 30 ps, which is selected as the TTM cutoff time for these simulations. This is demonstrated in Fig. 2 where the average electron and lattice temperatures within a 1000-nm-thick foil are plotted for the case of heating

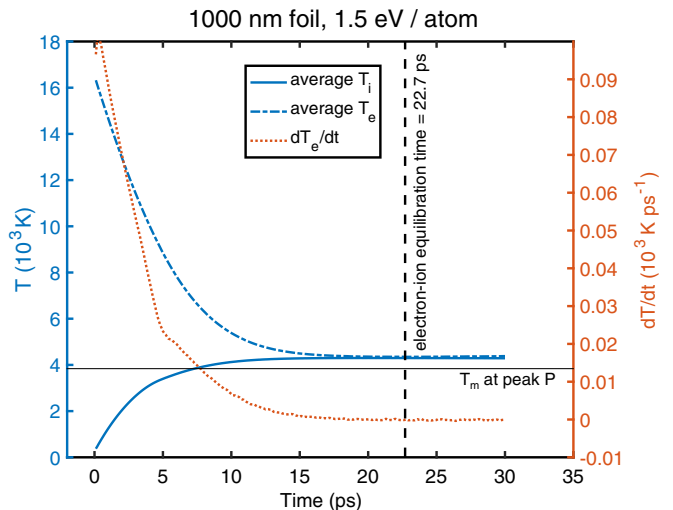


FIG. 2. Electron and lattice temperatures during the two-temperature model stage of the simulation for a 1000-nm-thick foil heated to 1.5 eV/atom. The temperature of each species is averaged over the initial dimensions of the foil. The solid blue curve is the average lattice temperature within the foil, while the dashed blue curve is the average temperature of the electron subsystem. The orange dotted curve on the right hand axis is the rate of change of the lattice temperature. The black horizontal line is the melting temperature for the EAM potential, at the value of peak pressure within the simulation. These diagnostics indicate that, at a time of 30 ps, the temperatures of the electron subsystem and the lattice have equilibrated, and the rate of lattice heating has slowed to zero.

to above the ablation threshold. The dashed blue and solid blue curves indicate the average electron and lattice temperatures within the foil, respectively. The solid horizontal line in Fig. 2 indicates the melting point measured for the embedded atom model (EAM) potential used in this study, at the peak value of hydrostatic pressure for this particular simulation (which is $P = 23.4$ GPa). The vertical dashed line corresponds to the time at which the average electron and lattice temperatures reach equilibrium. The average electron temperature decreases exponentially with time, with a characteristic $1/e$ timescale of 8.5 ps. The vertical line then indicates that electron-lattice temperature equilibration occurs within approximately 2.7 e -foldings. It is therefore appropriate to choose a cutoff time for the TTM module equal to 30 ps, or four e -foldings. In addition, the orange curve is the rate of lattice heating, which has slowed to approximately zero by 20 ps. These diagnostics confirm that the TTM module can be switched off at 30 ps without affecting the dynamics of the atoms, given that the lattice has reached thermal equilibrium with the electron subsystem by this time. Again it is important to stress that the selected TTM cutoff time of 30 ps is shorter than the typical hydrodynamic relaxation timescale, meaning that heating occurs under isochoric conditions.

Previous studies have utilized TTM-MD simulations to investigate ablation of metals under pulsed radiation. These may be grouped together, depending on the penetration depth of the incident radiation and the material under investigation. For example, Refs. [20,21,23,59] model the ablation of gold irradiated with weakly penetrating (optical or soft x-ray)

radiation, while Refs. [18,24] investigate ablation of thin gold foils in which uniform energy deposition is employed to simulate the role of ballistic electrons. Another commonly studied metal is nickel; for example, in Refs. [22,25] nickel ablation is investigated using short pulses of weakly penetrating radiation. The strength of the TTM-MD technique is reflected in the fact that the studies detailed in Refs. [19,21] found agreement between the predicted ablation threshold and the experimental measurement in gold. In addition, Ref. [1] reports that the predicted crater depth agrees with experimental measurements for both optical and soft x-ray irradiation of gold foil. However, it is important to note that the aforementioned studies have employed weakly penetrating radiation. A notable exception is Ref. [2], in which the possibility of structuring gold surfaces with high-energy x-rays is discussed. In that study, the absorption depth was 100 nm, corresponding to approximately 1-keV x-rays propagating in ambient density gold. However, current XFEL facilities are capable of delivering exceptionally bright pulses of hard x-rays with photon energies up to 25 keV, indicating a necessity to extend TTM-MD simulations to higher x-ray energies.

In this paper, we model the effect of the high-energy x-rays by increasing the absorption depth of the incident radiation [ℓ_s in Eq. (2)]. This is an attractive option for investigation given that it requires varying only the absorption depth and the incident intensity (to reach the desired level of lattice heating), and does not require modification of the source code to implement the high energy radiation. There is, however, a limit to this approach, in that the equations of the standard TTM do not address some of the complexities of hard x-ray matter interactions. For example, this approach does not explicitly account for nonthermal ballistic electrons within the metal. Here, the term nonthermal refers to the fact that the ballistic electrons are not in local thermal equilibrium with the finite heat reservoirs which comprise the electron subsystem. These ballistic electrons are seeded by intense x-ray irradiation and can carry heat much deeper into the metal than the absorption depth would imply. They are predicted to play an important role in studies of noble metals but a much lesser role for transition metals such as tantalum [60,61]. It is suggested in Refs. [18,24] that the effect of the ballistic electrons can be included by modifying the heat source term to give uniform energy deposition across the material, accounting for the deeper penetration of the heat.

Given the limitations detailed above, we restrict the x-ray energies in this study to the range 1–5 keV. These energies are still within the operating range of current XFEL facilities. Additionally, the pressure and temperature regime accessible in the simulations is comparable to the regimes reported in recent experimental and simulation-based studies (Refs. [27,39]), providing a point of comparison for our results.

As the fluence increases, photoionization effects (such as multiphoton and barrier suppression ionization [62]) also become important, which again are not included in TTM-MD simulations. This restricts the regime of validity to below the plasma formation threshold. However, we have no necessity to model these effects here, given that the mechanisms by which destruction of the foils occur (cavitation and subsequent ablation) are present well below the plasma formation threshold.

B. Simulation parameters

The simulations detailed in this paper are for freestanding tantalum foils, with thicknesses ranging from 150 nm to 1000 nm. In each case, the absorption depth (the depth at which the electron temperature decreases to $1/e$ of the peak value) is set equal to the foil thickness. As discussed in the Introduction, this approximates experimental conditions in which the foil thickness is chosen to be close to one absorption length for the incident radiation. Varying the absorption depth in this way is equivalent to changing the energy of the incident radiation. For the range of absorption depth values in this paper, the energy of the x-ray pulse is in the range 1.3–4.9 keV, estimated using data from Ref. [63].

The remaining pulse parameters are as follows. The pulse temporal profile is a top-hat function with a pulse duration of 100 fs. The LAMMPS TTM module requires the user to define the absorbed fluence, i.e., the fluence which is incident on the front surface of the foil. The fluence values in this paper are converted to an average atomic temperature in eV/atom. This enables the ablation threshold to be determined in terms of the average lattice temperature as opposed to stating the threshold as a fluence value, which depends on the absorption depth and foil thickness (although the fluence is also reported for convenience in the text). For each foil thickness, four simulations are run, corresponding to lattice heating to 0.95, 1.25, 1.5, and 2 eV/atom. This range captures heating from just below the melting point up to the predicted boiling point for the tantalum EAM potential, and therefore straddles the ablation threshold.

The simulations use the EAM potential developed by Ravelo *et al.* in Ref. [31]. EAM potentials are particularly well-suited to molecular dynamics simulations of a free-electron gas, since they account for many-body effects while maintaining a relatively low computational cost. It is reported that the computational cost of many-body potentials in molecular dynamics simulations scales linearly with the number of atoms [64]. This facilitates simulations with 10 s of millions of atoms, which are necessary in the current study, given the absorption depth of the hard x-rays under consideration is approximately one micron.

Laser-induced ablation involves a combination of quantum (laser absorption and electron-phonon coupling) and classical (hydrodynamic release, melting, and tensile strength) processes, meaning that it is extremely difficult to locate a potential which accurately captures all the underlying physics. We tested a range of tantalum EAM potentials in preliminary simulations, however, the Ravelo Ta2 potential was determined to perform best for this investigation. Two important considerations are the fact that the Ravelo Ta2 potential gives a smooth variation of the Grüneisen parameter as a function of volumetric compression, even at the high pressures and temperatures accessible in this study, and that the melt curve for this potential is in agreement with experimental data obtained from diamond anvil cell studies. The experimental results against which this potential are validated extend up to 100 GPa, as described in Ref. [49]. It is worth noting that the Ravelo Ta2 potential underestimates the Grüneisen parameter by approximately 40% at ambient conditions, which will subsequently have an effect on the thermal expansion

coefficient of tantalum [33]. However, it is reported in Ref. [33] that the average value of the Grüneisen parameter from the simulations in the pressure range 0–100 GPa is close to the average over the corresponding experimental data. Again, we stress that the robustness of the Ravelo Ta2 potential in the high-pressure regime, and its demonstrable ability to recreate the thermal properties of tantalum, make it a suitable choice for this study.

In TTM-MD simulations, it is necessary to specify the form of the electron heat capacity, c_e , and electron thermal conductivity, κ_e . Here, we assume the free-electron gas model, in which the electron heat capacity varies linearly with electron temperature, T_e . This linear approximation is typically valid up to the Fermi temperature, and indeed the peak electron temperatures reached in this study are well below this limit. It follows that $c_e = \gamma T_e$, where $\gamma = 77.4 \text{ Jm}^{-3} \text{ K}^{-2}$. In LAMMPS, the electron thermal conductivity is related to the electron heat capacity through the thermal diffusion constant, D_e , such that $\kappa_e = D_e c_e$. The thermal diffusion constant is defined as follows:

$$D_e = \frac{K_0}{\gamma T_a}, \quad (4)$$

where $K_0 = 57.6 \text{ Wm}^{-1} \text{ K}^{-1}$ is a constant, obtained from Ref. [65] and T_a is the atomic (lattice) temperature. The chosen value of K_0 likely leads to an underestimate of the electron thermal conductivity, as noted in Ref. [66], however, more recent calculations in Ref. [67] show that our value is only a factor of 2 lower than the theoretical prediction under equilibrium conditions. It is demonstrated in Ref. [67] that the electron thermal conductivity of tantalum has a nonlinear dependence on T_e . Given that LAMMPS relates the thermal conductivity to the heat capacity via the thermal diffusion constant, it is not possible to implement an electron thermal conductivity with a different functional form to that of the electron heat capacity (which Ref. [67] shows is indeed the case), without modification of the source code. We therefore chose the K_0 value described above and leave detailed investigations of the effect of nonlinear electron thermal conductivity for future work. The final thermodynamic parameter is the electron-phonon coupling constant, $G = 3.08 \times 10^{17} \text{ Wm}^{-3} \text{ K}^{-1}$, obtained from Ref. [58].

The freestanding foils comprise a bcc lattice with 60×60 unit cells in the transverse dimensions, and 453–3027 unit cells in the longitudinal (x-ray pulse propagation) direction, depending on the foil thickness. The transverse dimensions of the simulation box greatly exceed the predicted critical void diameter (detailed in the Appendix) and so the growth of supercritical voids is uninhibited by the simulation size. We also note that the ablation threshold, which occurs when a void reaches a size comparable to the transverse dimensions, is reported to have a dependence on the simulation size [19,68,69]. In contrast, we report that the cavitation threshold (the fluence at which voids appear) is consistent provided the transverse dimensions exceed the critical void diameter, and has been confirmed during convergence testing of our simulation setup.

The simulation effectively models heat conduction only along the x-ray pulse propagation direction. Given that the x-ray pulses employed experimentally typically have a Gaussian spatial profile with full width half maximum diameter

$\approx 10 \mu\text{m}$, and the transverse dimension of the foil in the simulation is 19.8 nm, there will be negligible lateral heat transport. This justifies the 1D heat conduction model employed in this investigation. The foil sits in the middle third of the simulation box, with vacuum regions on either side, equal to the foil thickness. The simulation box has periodic boundaries in the transverse dimensions and nonperiodic boundaries in the longitudinal direction. The simulation box is overlaid with a grid on which the electron subsystem is defined, where each cell in the grid has a longitudinal extent of 1 nm.

Each simulation is run for sufficiently long that the rarefaction waves propagating from the free surfaces have time to interfere and create a region of peak tension. For the 150-, 300-, and 500-nm-thick foils, a run time of 200 picoseconds (ps) is sufficient, however, for the 1000 nm simulations the run time is extended to 400 ps. In every case, the MD time step is equal to 1 fs, which is sufficient to generate smooth atomic trajectories while incurring a minimal computational cost.

Finally, we comment on the notation used to report the hydrodynamic variables from the simulations. LAMMPS enables the computation of the components of the stress tensor for each individual atom. The output quantity has units of pressure multiplied by volume, so to obtain a pressure value it is necessary to divide through by the per-atom volume. This quantity is estimated from the simulations by calculating the volume of the Voronoi tessellation around each atom. The spatial profile of each stress tensor component is then computed by binning the per-atom values across the simulation box, summing the values within each bin, and dividing by the sum of the per-atom volumes within the bin. The hydrodynamic pressure, P , is related to the diagonal components of the stress tensor via Eq. (5), below:

$$P = -\frac{1}{3}(\sigma_{xx} + \sigma_{yy} + \sigma_{zz}). \quad (5)$$

The x-ray pulse propagates along the simulation x axis, which is also the axis of pressure release. Throughout this paper, we report the value of hydrostatic pressure when the tensile stress within the foil reaches its peak magnitude. From Eq. (5), this results in negative values of pressure. We also report the values of the components of the stress tensor noting that in the liquid phase, $\sigma_{xx} \approx \sigma_{yy} \approx \sigma_{zz}$, and that $P \approx -\sigma_{xx}$.

IV. RESULTS

A. 150-nm freestanding foil

The first results presented are from four simulations with a 150-nm-thick freestanding foil heated to 0.95, 1.25, 1.5, and 2 eV/atom, respectively. The 150-nm foil is sufficiently thin that heat is carried across the extent of the target during the electron-lattice equilibration stage. This results in uniform heating, with the electrons and lattice reaching thermal equilibrium by 30 ps. This is demonstrated in Fig. 3, where the temperature profiles are plotted for the case of heating to 2 eV/atom (corresponding to a fluence of 2700 Jm^{-2}). The solid blue and dashed blue curves correspond to the electron and lattice temperatures at the foil front surface. The solid red and dashed red curves correspond to the same quantities on the rear surface. Figure 3 demonstrates that by 25 ps, the lattice front and rear temperatures have reached equilibrium. This lattice temperature sits well above the melting point of

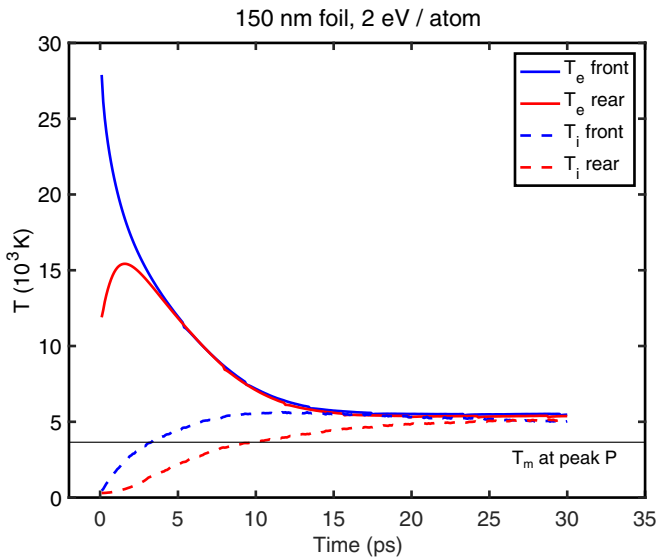


FIG. 3. Temperature profiles for a 150-nm freestanding foil heated to 2 eV/atom. The solid blue and dashed blue curves correspond to the electron and lattice temperatures measured at the foil front surface. The electron and lattice rear temperatures are plotted with solid red and dashed red lines, respectively. The horizontal line is the melting temperature for the EAM potential at the value of peak pressure in the simulation.

the EAM potential (measured at the value of peak pressure within the sample, indicated by the horizontal black line). As discussed in the previous section, the TTM module is switched off at 30 ps, given that the rate of lattice heating approaches zero.

The peak tensile stress which can be achieved in the 150-nm-thick foil is limited by the fact that the condition for heating under stress confinement is only weakly met. As described in Ref. [25], the stress confinement condition is that the radiation pulse duration and the electron-lattice equilibration time must be less than the timescale of thermal expansion, obtained by dividing the foil thickness by the speed of sound. Estimating the speed of sound from the simulation as 3479 ms^{-1} (which is in agreement with the ambient density value of $\approx 3400 \text{ ms}^{-1}$ from Ref. [51]), the timescale for thermal expansion is approximately 40 ps, comparable to the electron-lattice equilibration time of 30 ps. Given that the stress confinement condition is only just met, a larger fraction of the foil will have relaxed over the timescale of electron-lattice equilibration compared to the thicker foils. In this case, a relatively low thermal pressure builds within the foil which, upon release, generates tension with a small magnitude. It is not until heating to 2 eV/atom that evidence of cavitation appears in the simulations.

Space-time plots of the density, pressure, and lattice temperature evolution are included in Fig. 4 for two different levels of heating. In Figs. 4(a)–4(c), heating occurs to 1.5 eV/atom (at a fluence of 1995 Jm^{-2}), whereas Figs. 4(d)–4(f) correspond to heating to 2 eV/atom. First, looking at the temperature profile in Fig. 4(c), it is evident that the front and rear surfaces of the foil have reached a similar temperature, just exceeding the melting point of the EAM potential. It is inferred that at this point in the interaction the foil is molten, however, further evidence is provided in the Appendix, Fig. 15, where the melting of the lattice is corroborated by a broadening of simulated x-ray diffraction (XRD) peaks. Figure 4(c) also shows there is some periodicity in the

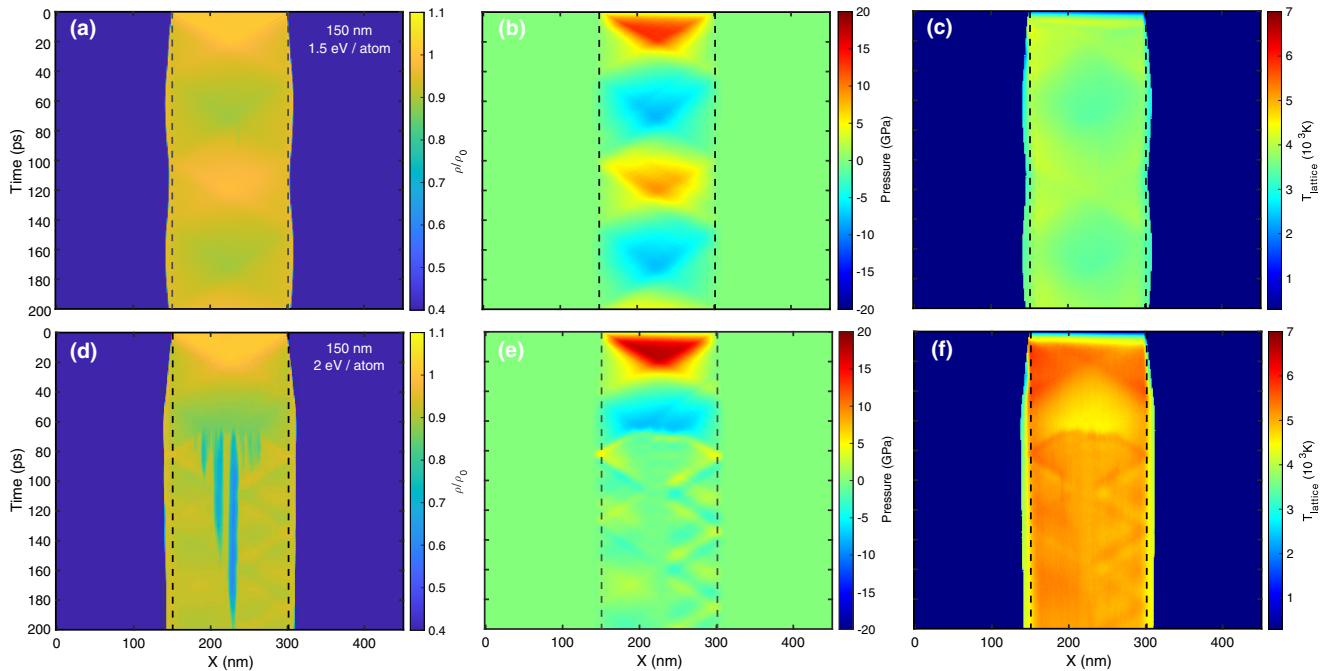


FIG. 4. Space-time plots of the density, pressure, and lattice temperature for a 150-nm freestanding tantalum foil. (a)–(c) correspond to average lattice heating to 1.5 eV/atom, while the heating is to 2 eV/atom in (d)–(f). The black dashed lines in each case indicate the initial foil boundaries. (d) shows the formation of multiple voids within the foil as it is heated to 2 eV/atom. These voids do not reach the critical size necessary for ejection of material and subsequently collapse, with the largest void vanishing just before the end of the simulation.

temperature as a function of time, coincident with oscillations in the pressure and density, due to hydrodynamic reverberations.

The density space-time profile plotted in Fig. 4(a) shows that the rarefaction waves, traveling from the free-surfaces inward, begin to overlap at approximately 40 ps. Looking at the space-time profile of the pressure in Fig. 4(b), it is clear that tension forms within the foil at this time, when the rarefaction waves intersect. The peak tension (i.e., the greatest magnitude of σ_{xx}) is reached at the center of the foil at a time of 70 ps. However, it is not sufficient at this time to exceed the tensile strength of the material, and the pressure waves continue to reverberate within the foil. The frequency of these oscillations is high compared to the thicker foils, since the pressure waves can traverse the thinner foil more quickly. Comparing Figs. 4(a) and 4(b), the pressure oscillations coincide with oscillations in the density; the high-density regions align with those of positive hydrodynamic pressure, and vice versa.

As the heating increases to 2 eV/atom, the peak thermal pressure within the foil increases. The release of this pressure results in tension which is sufficient in magnitude to lead to cavitation. The value of hydrodynamic pressure at the time of maximum tension (σ_{xx} reaches its peak value at time $t = 62.5$ ps) is $P = -7.63$ GPa. Since the foil is molten at this time, the components of the stress tensor have similar values of $\sigma_{xx} = 7.78$ GPa, $\sigma_{yy} = 7.59$ GPa, and $\sigma_{zz} = 7.53$ GPa. Interestingly, we observe anisotropy in the pressure tensor components under weaker heating to 0.95 eV/atom, where the lattice temperature sits below the EAM melting point. In that case, the values of σ_{xx} , σ_{yy} , and σ_{zz} are 4.79, 3.32, and 3.43 GPa, respectively.

Strong evidence of cavitation is provided in Fig. 4(d), where a large void appears near the center of the foil at a time of 70 ps, and remains until around 190 ps. The location of this void coincides with the peak tensile stress, further hinting that cavitation is the mechanism underlying failure of the foil. The general trend for the 150-nm foils is that the magnitude of tensile stress increases with the level of heating. The pressure at the time of maximum tension varies from -3.85 GPa to -7.63 GPa as the heating increases from 0.95 to 2 eV/atom.

There is also evidence of additional, smaller voids forming around the largest void. Again, these are seeded in the relatively wide region of tensile stress around the center of the foil. These satellite voids which are visible in Fig. 4(d) collapse at later times and do not lead to ejection of material layers. The sections of material which are separated by these voids subsequently act as independent foils, since void formation results in additional free surfaces.

Finally, we comment in more detail on the dynamics underpinning the failure of the foil. The density space-time plot in Fig. 4(d), and further visualization of the atomic positions, demonstrate that all the voids collapse before the end of the simulation. Despite having a radius greater than the predicted critical value, the reverberating pressure waves likely trigger the void collapse and we do not see ablation, which arises when the voids grow to a size comparable to the transverse dimensions of the simulation box. We conclude that the cavitation threshold for the 150-nm foil occurs at 2 eV/atom, but the voids which form do not lead to splitting of the foil.

B. 300-nm freestanding foil

In contrast to the 150-nm-thick foil, the 300-nm foil is sufficiently thick that thermal conduction cannot equalize the lattice temperatures at the front and rear of the foils. This asymmetry in the heating leads to a temperature and stress gradient through the foil. The increased absorption depth in this case also means that a larger volume of the foil remains under stress confinement at the electron-lattice equilibration time. This results in the release of a larger thermal pressure, inducing a state of tension with greater magnitude relative to the 150-nm-thick foil.

Space-time plots of the density, pressure, and lattice temperature are provided in Fig. 5. The vertical dashed black lines indicate the initial foil boundaries. Figures 5(a)–5(c) show the case of average lattice heating to 1.25 eV/atom (corresponding to a fluence of 3400 Jm^{-2}). This is considered to be the cavitation threshold for the 300-nm simulations, as Figs. 5(a) and 5(b) clearly show void formation by 130 ps. Increasing the level of heating further results in the growth of supercritical voids and subsequent ablation of the foil. Comparing the density plot to the pressure plot in Figs. 5(a) and 5(b), the location of the void coincides with the peak tensile stress. The asymmetry in the heating is apparent in the space-time plot of the lattice temperature, where the irradiated side of the foil is hotter than the rear, as well as in the density profile in Fig. 5(a) in which the rarefaction wave launched from the front surface results in a greater decrease in density relative to the rear.

Upon heating to 1.25 eV/atom, the pressure value is $P = -9.43$ GPa, compared to -6.22 GPa in the 150-nm foil at the same level of heating. This is the greatest magnitude of tension of any of the 300-nm simulations, a characteristic which indicates that this level of heating corresponds to the cavitation threshold [25]. This also coincides with the stress tensor components reaching approximately equal values. Below the cavitation threshold, at 0.95 eV/atom, the stress tensor components show slight anisotropy with σ_{xx} , σ_{yy} , and σ_{zz} taking values of 6.8, 5.22, and 5.27 GPa, respectively. At the cavitation threshold, the values of σ_{xx} , σ_{yy} , and σ_{zz} are comparable at 9.61, 9.3, and 9.39 GPa, respectively.

Despite the fact that a void is seeded at 130 ps, it subsequently collapses approximately 60 ps later. This behavior is also illustrated in the phase diagram, the inset in Fig. 6. The thermodynamic trajectory in density-temperature space is plotted for different levels of heating, with the red circles corresponding to the 1.25 eV / atom case. The thermodynamic parameters are averaged over a region of four unit cells near the center of the foil. The density is calculated by summing the mass of the atoms within the slice and dividing by the sum of the per-atom volumes (the volume of the Voronoi tessellation associated with each atom). The resulting trajectory provides a macroscopic view of the system as it excludes the presence of voids. This removes the bias which could occur if the sampled region contained a large volume of voids, in which case the density of the region would be underreported (and the trajectory would penetrate deeper into the vapor dome), assuming the volume in the density calculation is that of the entire slice. The average temperature within the slice is calculated from the sum of the per-atom kinetic energies using equipartition theory. For each trajectory in Fig. 6, the color

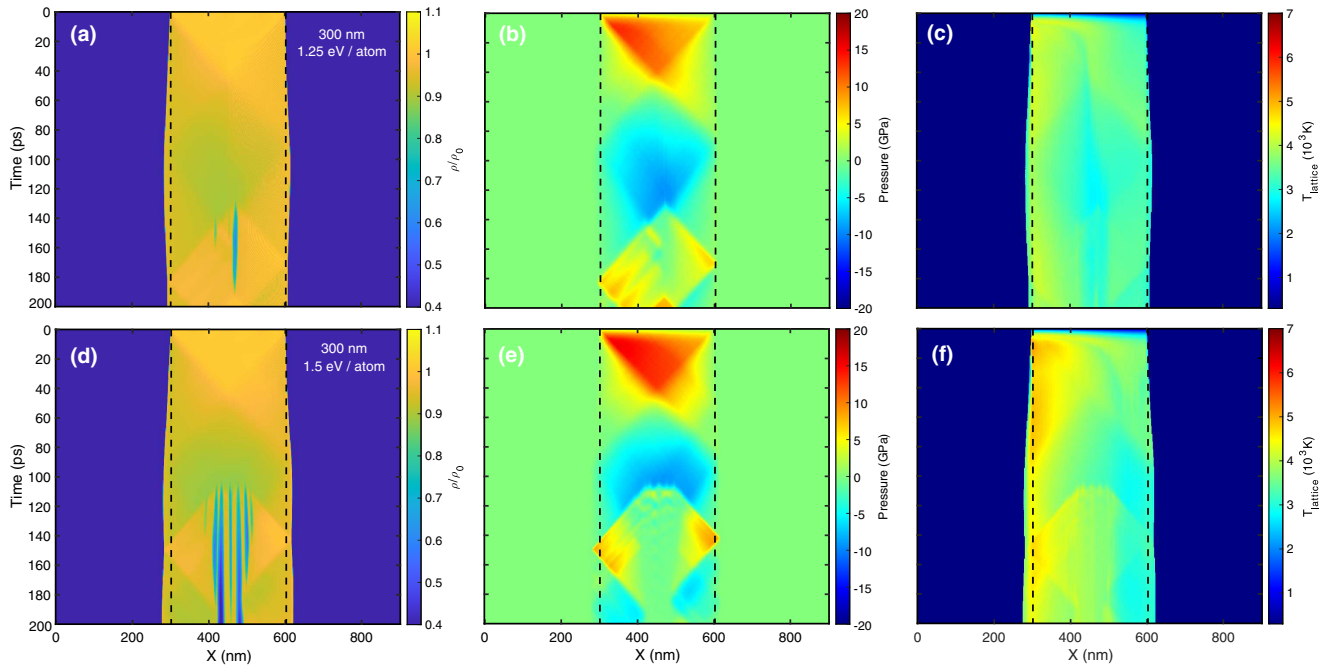


FIG. 5. Space-time plots of the density, pressure, and lattice temperature for a 300-nm freestanding tantalum foil. (a)–(c) correspond to average lattice heating to 1.25 eV/atom, while the heating is to 1.5 eV/atom in (d)–(f). The dashed black lines indicate the initial foil boundaries. (a) demonstrates void formation and collapse upon heating of the foil to 1.25 eV/atom. As the heating increases to 1.5 eV/atom in (d), void nucleation occurs at an accelerated rate. Here, multiple voids reach the critical size and cause separation of material layers. Comparing (d) and (e), it is clear that the region of void formation coincides with the region of peak tensile stress.

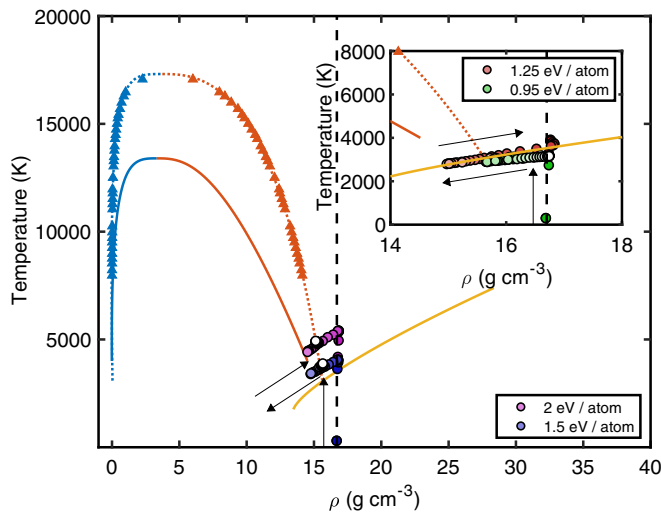


FIG. 6. Plot of the thermodynamic trajectory, averaged across a slice of length four unit cells, close to the center of the 300-nm-thick foil. The density calculation excludes the presence of voids and provides a macroscopic view of the system. The phase boundaries follow the same descriptions as in Fig. 1. The purple and blue circles in the main plot are points along the thermodynamic trajectory of the central region, upon heating to 2 eV/atom and 1.5 eV/atom, respectively. The fading of the colors in the data points, and the black arrows, denote the passage of time. The inset shows the trajectory for cases where the lattice is heated to 1.25 (red circles) and 0.95 (green circles) eV/atom, respectively, over a smaller region of phase space. For the lowest level of heating, the trajectory is mostly below the melt curve. This indicates cavitation is unlikely to occur given that this is defined as the failure of a liquid under tension.

fades toward white as time progresses, with the black arrows further illustrating the passage of time. The trajectory for the 1.25 eV/atom case initially crosses the melt curve during the pressure release stage. It then hovers around the melt curve during the pressure release stage, moving into the vapor dome at a time of 120 ps. The reverberation waves push the trajectory back out of the vapor dome, leaving it in a molten state just above the melt curve. This behavior is consistent with Fig. 5(a), where the initial void growth coincides with the atoms entering the vapor dome, and void collapse is indicated by the atoms crossing back over the vapor dome boundary and into the liquid region of the phase diagram.

It is important to note that as the molten material crosses the vapor-dome boundary it is a mixture of phases, which have different densities and temperatures. The phases are separated by analyzing the Voronoi cell volumes of atoms with a density less than the value at the critical point (as reported in the Appendix). Taking the example of heating to 1.5 eV/atom, we report the gaseous phase appears at 105 ps (corresponding to the average trajectory entering the vapor dome), with a density of 2.5 g cm^{-3} and a temperature of 4960 K. This differs from the average properties of the mixed phase, of 14.8 g cm^{-3} and 3420 K, at the same time in the simulation. The presence of the mixed phase again highlights that destruction of the foil occurs via cavitation, as opposed to spallation which requires the sample remain in the solid phase.

As the lattice heating increases to 1.5 eV/atom (corresponding to a fluence of 3900 Jm^{-2}), the foil is again heated above the melting point. This is demonstrated in Fig. 5(f), which shows the space-time plot of the lattice temperature. In this case, it is more evident that there is a temperature

gradient across the foil, with heating on the irradiated side leading to an increase in the thermal pressure in this region. For this level of heating, the magnitude of tension decreases relative to the 1.25 eV/atom case. The pressure reaches a value of $P = -9.33$ GPa, and given that the foil is molten, the components of the pressure tensor have similar values of σ_{xx} , σ_{yy} , and σ_{zz} equal to 9.35, 9.38, and 9.27 GPa, respectively.

Void formation occurs at later times (>100 ps) within the region of tension created by the intersection of the rarefaction waves from the front and rear surfaces. In contrast to the 1.25 eV/atom case, multiple voids of critical size are seeded within the foil, which remain throughout the simulation. After void formation occurs, the pressure in the void location jumps from a negative value to zero. In Fig. 5(e), it is clear that pressure reverberations continue within the regions of the foil which are separated by voids. Heat conduction is also stopped across these sections, leading to higher lattice temperature in the section of foil closest to the side of irradiation.

It is likely that cavitation is the ablation mechanism present in the 300-nm simulations. The phase diagram in the main body of Fig. 6 supports this conclusion, given that the phase space trajectories for the cases of heating to 1.5 and 2 eV/atom (denoted by blue and purple circles, respectively) remain above the EAM melt curve at the end of the simulation. Note that for cavitation to occur, the trajectory must cross the melt curve, given that this process is described as the failure of a liquid under tension. Our prediction that the ablation mechanism is cavitation is then supported by the fact that for all cases where ablation occurs, the thermodynamic trajectory does indeed cross the melt curve and enter the vapor dome, where voids can be seeded. In fact, for the cases of heating to 1.5 and 2 eV/atom, the trajectories remain within the vapor dome at the end of the simulation, which allows the possibility of a high rate of void nucleation.

In contrast to photothermal ablation mechanisms (such as vaporization), cavitation and spallation are driven by tensile stress. To further demonstrate that tensile stress plays an important role in the failure of the 300-nm foils, the spatial profile of the hydrodynamic pressure is plotted in Fig. 7. At 2 ps, following the x-ray pulse, the irradiated side of the foil is heated and consequently reaches $P \approx 5$ GPa (demonstrated by the blue curve). The asymmetry in the heating is evident by the factor of 2 difference in the values of hydrodynamic pressure at the front and rear of the foil. At 16 ps (the orange curve), a significant region of the foil is still under stress confinement and continues to heat during the electron-lattice equilibration stage. The pressure has already started to decrease near the foil boundaries, indicating the expansion of the free surfaces into vacuum and the propagation of rarefaction waves into the bulk. The peak tension forms at 100 ps, as indicated by the yellow curve, followed by void formation near the center of the foil. After void formation, the pressure value in the vicinity of the void jumps from highly negative to zero, as indicated in the spatial profile at 109 ps (the purple curve in Fig. 7).

C. 500-nm freestanding foil

As the target thickness increases to 500 nm, we again have nonuniform heating resulting in pressure and temperature gradients across the foil. This is demonstrated in the space-time

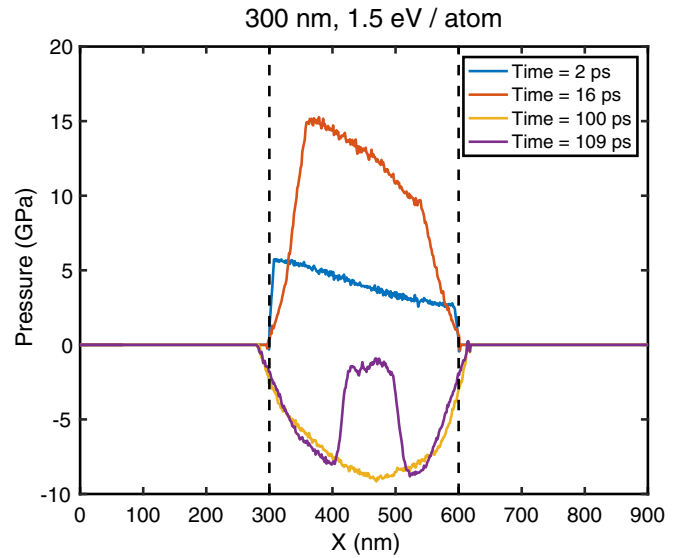


FIG. 7. Line out of hydrodynamic pressure at selected times, from a simulation with a 300-nm freestanding tantalum foil heated to 1.5 eV/atom.

plots of the pressure and lattice temperature, for the case of heating to 1.25 eV/atom (at a fluence of 5500 Jm^{-2}), in Figs. 8(b) and 8(c). The ablation threshold for the 500-nm simulations is, again, 1.25 eV/atom. This is confirmed in the space-time plot of the density in Fig. 8(a) by the appearance of a critically sized void at approximately 150 ps. The late onset of void formation, relative to the thinner foil simulations, is due to the increased time it takes for the rarefaction waves from the front and rear surfaces to intersect and form tension within the foil.

Comparing the density and pressure plots in Figs. 8(a) and 8(b), it is clear that the void forms in a region of tension. However, an interesting additional feature emerges, in that the region with the largest magnitude of tensile stress is spatially separated from the void formation region. The purple triangles mark the position and time at which the magnitude of tension reaches its peak. The first void appears at 150 ps, at position $X \approx 700$ nm, whereas the peak tension forms 40 ps later at a position of $X \approx 850$ nm. This behavior is reported in Ref. [25] for TTM-MD simulations of ablation in nickel foils. We now confirm the same response for tantalum, via simulations of freestanding foils of greater thickness than those in Ref. [25] (although we also note that Ref. [25] reports the same behavior in a bulk foil, where heat conduction occurs deep into the material). The separation of the regions of peak tensile stress and void formation is the result of thermal softening. The material on the irradiated side of the foil is hotter (due to the temperature gradient) and therefore supports a weaker magnitude of tensile stress. This is relative to the rear of the foil, which is ≈ 1000 K cooler throughout the simulation, and therefore supports a larger magnitude of tension.

As the level of heating is increased to 1.5 eV/atom (corresponding to a fluence of 6650 Jm^{-2}) in Figs. 8(d)–8(f), the effect of thermal softening becomes more apparent. The spatial separation between the first void and the region of peak tensile stress is increased to 219 nm, with a temporal

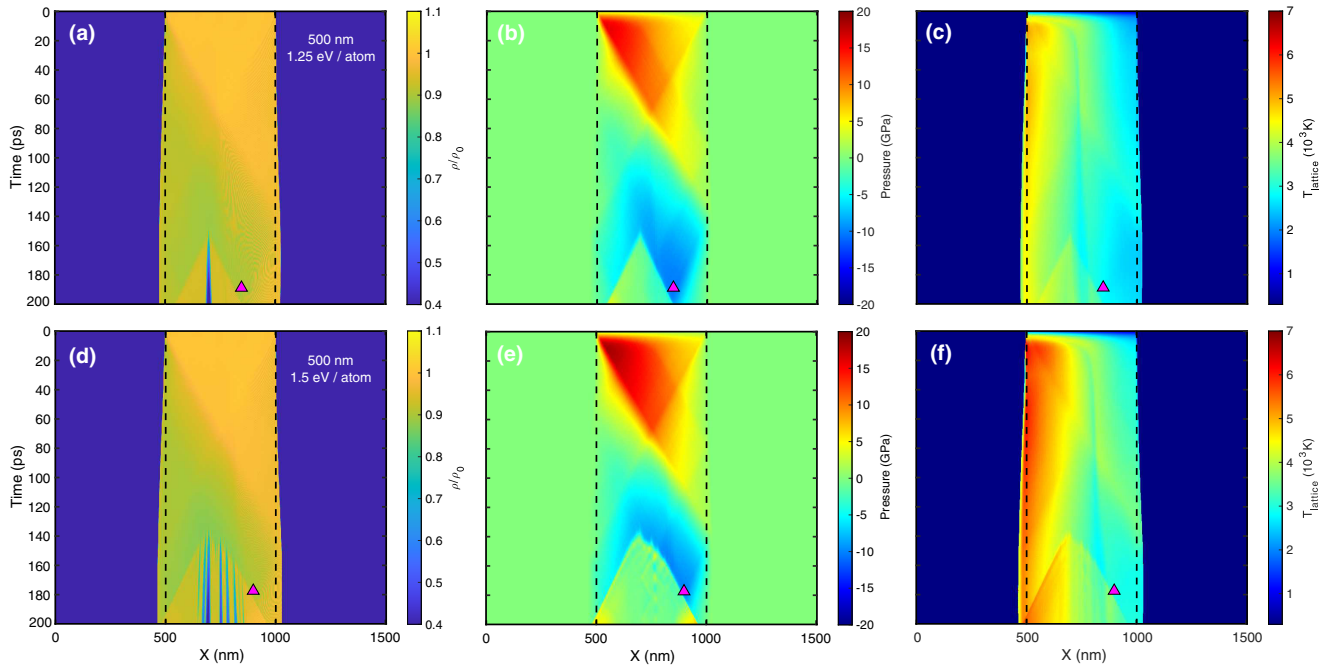


FIG. 8. Space-time plots of the density, pressure, and lattice temperature for a 500-nm freestanding tantalum foil. (a)–(c) correspond to average lattice heating to 1.25 eV/atom, while the heating is to 1.5 eV/atom in (d)–(f). The dashed black lines in each case indicate the initial foil boundaries, while the purple triangles mark the position and time at which the tensile stress reaches its maximum magnitude. (a) and (d) indicate that heating to ≥ 1.25 eV/atom is sufficient to induce cavitation, with voids appearing and remaining throughout the simulations.

separation of ≈ 40 ps, as indicated by the location of the purple triangle relative to the location of the first void. While Fig. 8(f) demonstrates a significant thermal gradient across the foil, another striking feature is the cooling which occurs near the center. This cooling starts around 20 ps and continues at this location until void formation begins at approximately 150 ps. We probe this region by employing additional diagnostics, including analysis of the phase space trajectory and simulated XRD patterns. The purpose of the additional analysis is to determine the state of the material at the center of the foil, which in turn provides information on the ablation dynamics.

The positions and times captured by the additional diagnostics are marked in Fig. 9(a) by colored triangles. First, we look at a thermodynamic trajectory in density-temperature space, which is representative of the macroscopic state of the system (corresponding to the average density and temperature of the mixed phase). This is plotted as a function of time at a constant position ($X = 814.4$ nm) in Fig. 9(b). The 500-nm-thick foil is heated under the condition of stress confinement to approximately 3800 K, which is above the melt curve for the EAM potential. The peak lattice temperature occurs at 30 ps, when the lattice and electron subsystem reach equilibrium. The sampled volume remains stress confined at 50 ps, after which time the thermal pressure begins to release. During the subsequent cooling, the trajectory remains just above the EAM potential melt curve. At 100 ps, the rarefaction waves from the free surfaces begin to intersect, with the associated decrease in density pulling the thermodynamic trajectory into the vapor dome. At 150 ps, voids begin to form around the sampled region due to high tensile stress. This void formation causes release of tension and an increase in density as the trajectory propagates toward the liquid region

of the phase diagram. The subsequent pressure reverberations cause the trajectory to oscillate between the liquid region of the phase diagram and the vapor dome toward the end of the simulation. We note that while the average parameters of the mixed phase are plotted in Fig. 9(b), it is also possible to comment on the gaseous phase which appears at 150 ps. The density of this phase is 1.79 g cm^{-3} at this time and the temperature is 7900 K.

This behavior is also reflected in the simulated XRD patterns in Fig. 9(c). The XRD data is obtained using a custom package in LAMMPS, with further details provided in the Appendix. The XRD calculation samples a volume of $15 \times 15 \times 15$ unit cells at locations centered on the colored triangles in Fig. 9(a). The black diffraction pattern corresponds to ambient conditions ($t = 0$ ps, with the initial lattice equilibrated to 300 K), where it is clear that there are strong peaks associated with the labeled Miller planes. The ambient peaks are still visible at 30 ps (the end of the TTM stage) and at 50 ps, although the intensity of the signal is weaker, consistent with melting of the lattice. At 100 ps and 150 ps (plotted in the inset), the only significant peak is from the (110) planes. Again, there is strong evidence of peak broadening, and the position of the peak has shifted compared to the ambient XRD pattern, suggesting the foil is under tension. Given the broad liquid background, we suggest that the cooling at the center of the foil does not result in a transition back to the solid state. The XRD patterns are in agreement with analysis of the thermodynamic trajectory, indicating the foil remains above the melt curve.

Finally, we comment on the ablation mechanism for the 500-nm foils. Figure 8(d) demonstrates that, upon heating to 1.5 eV/atom, there is an increased rate of void nucleation,

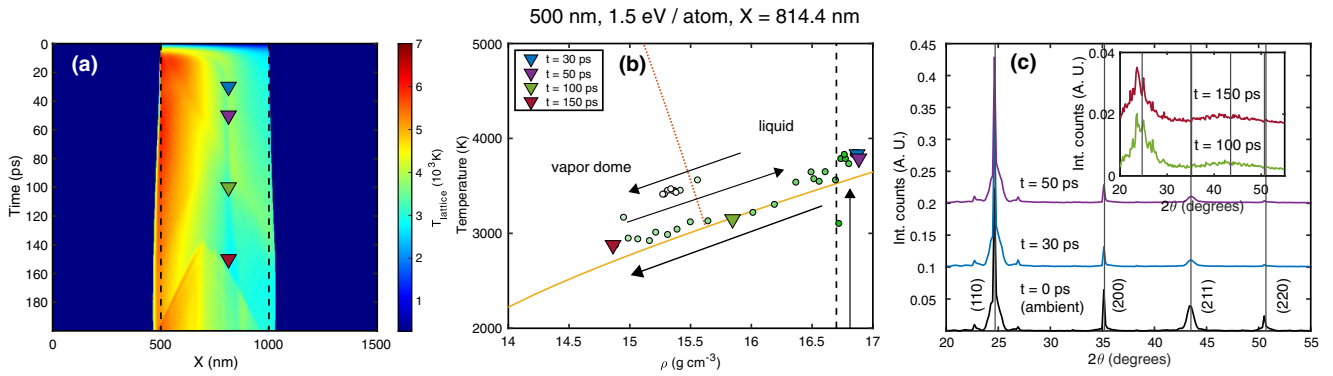


FIG. 9. (a) The space-time plot of the lattice temperature for the 500-nm-thick foil, heated to 1.5 eV/atom, is supplemented with additional diagnostic data. The triangles in (a) indicate the positions and times at which additional data are obtained. The thermodynamic trajectory in density-temperature space for a region of length four units cells, centered on position $X = 814.4$ nm (at times corresponding to the times indicated by the colored triangles), is plotted with green circles in panel (b). The phase boundaries are the same as those described in Fig. 1 and the black arrows indicate the passage of time. Synthetic x-ray diffraction profiles are plotted in (c). The black profile is the diffraction pattern at ambient conditions, while the colors of the additional profiles correspond to the colored triangles in (a), indicating the position and time at which the data is obtained. The diffraction patterns at 100 and 150 ps are plotted in the inset with an adjusted vertical scale to emphasize the broad liquid peaks. The vertical lines in (c) denote the 2θ diffraction angles associated with reflection from the Bragg planes indicated by the (h,k,l) indices marked at the bottom of each line. The broad XRD profiles suggest that the crystal remains molten, despite the cooling which occurs near the center of the foil.

which could be indicative of explosive boiling. However, visualization of the atomic positions reveals that the boundary between the hot material and vacuum remains sharp. In contrast, it is reported in Refs. [25,69] that explosive boiling is characterized by the decomposition of the material-vacuum interface into fluid clusters, surrounded by gaseous atoms. This conclusion, that the ablation mechanism is cavitation for the 500-nm simulations, is supported by the preceding analysis of the thermodynamic trajectory. Even at high fluence values, the transition across the binodal line occurs well below the critical point. As discussed in Sec. II, explosive boiling typically occurs when the material is heated close to the critical temperature.

D. 1000-nm freestanding foil

The thickest foil under consideration in this study is 1000 nm, corresponding to the penetration depth for a 4.7 keV photon in ambient density tantalum. Given the increased thickness, the time required for the counterpropagating rarefaction waves from the front and rear surfaces to intersect increases, from approximately 150 ps for the 500-nm-thick foil to 250 ps in the 1000-nm-thick case. The simulation run time is increased accordingly, from 200 to 400 ps.

The density, pressure, and temperature profiles are plotted in Figs. 10(a)–10(c) for heating to 1.25 eV/atom (corresponding to a fluence of $11\,000\text{ Jm}^{-2}$), which is the cavitation (and ablation) threshold. It is important to highlight that this threshold is the same as for the 300-nm and 500-nm foils. The reason for the consistency in the behavior is that these target thickness values exceed the distance over which the heat is carried through the target. This leads to a temperature gradient across the foil, however, the ratio of the absorption depth to the target thickness is maintained at 1:1 and so the gradient is comparable in all cases. In contrast, while the same 1:1 ratio is present in the 150-nm foil, thermal conductivity equalizes

the front and rear temperatures and there is no thermal or pressure gradient across the foil. Failure of the 1000-nm foil upon heating to 1.25 eV/atom is demonstrated in Fig. 10(a), with a critically sized void forming at $X = 1375$ nm after 225 ps. The location of the peak magnitude of the tensile stress (indicated by the purple triangle) is spatially separated from the location of the first void appearing in the foil, due to thermal softening. The pressure profile also demonstrates that stress confinement is satisfied across a larger volume of this thicker foil, with approximately no pressure release due to free-surface expansion until at least 30 ps.

Figures 10(d)–10(f) correspond to heating to 2 eV/atom, where the rate of void nucleation is seen to increase with the level of heating. This is evinced by the fact that at least eight voids appear throughout the bulk of the foil upon heating to 2 eV/atom, whereas only two voids are present at 1.25 eV/atom. This suggests thermal softening plays an important role, where the ability to support a smaller magnitude of tensile stress triggers failure multiple times within the foil. Some of these voids are seeded with insufficient energy to grow over time, while others merge with neighboring voids and achieve the critical size.

In Fig. 10(f), we see that the lattice temperature in the void formation region exceeds the boiling point predicted for the EAM potential. Closer inspection of the voids shows that they contain very few gaseous atoms and there is still a clear boundary between regions which are separated by the formation of voids. This suggests that ablation is driven by mechanical means up to at least the boiling point, and that the effects of thermal processes such as explosive boiling are negligible even at this high level of heating (to 2 eV/atom). This is also consistent with the thermodynamic trajectories in density-temperature space, which show ablation occurs when the trajectory enters the vapor dome. As noted in Sec. II, it is generally understood that phase explosion requires heating to approximately 90% of the critical temperature. Analysis of the

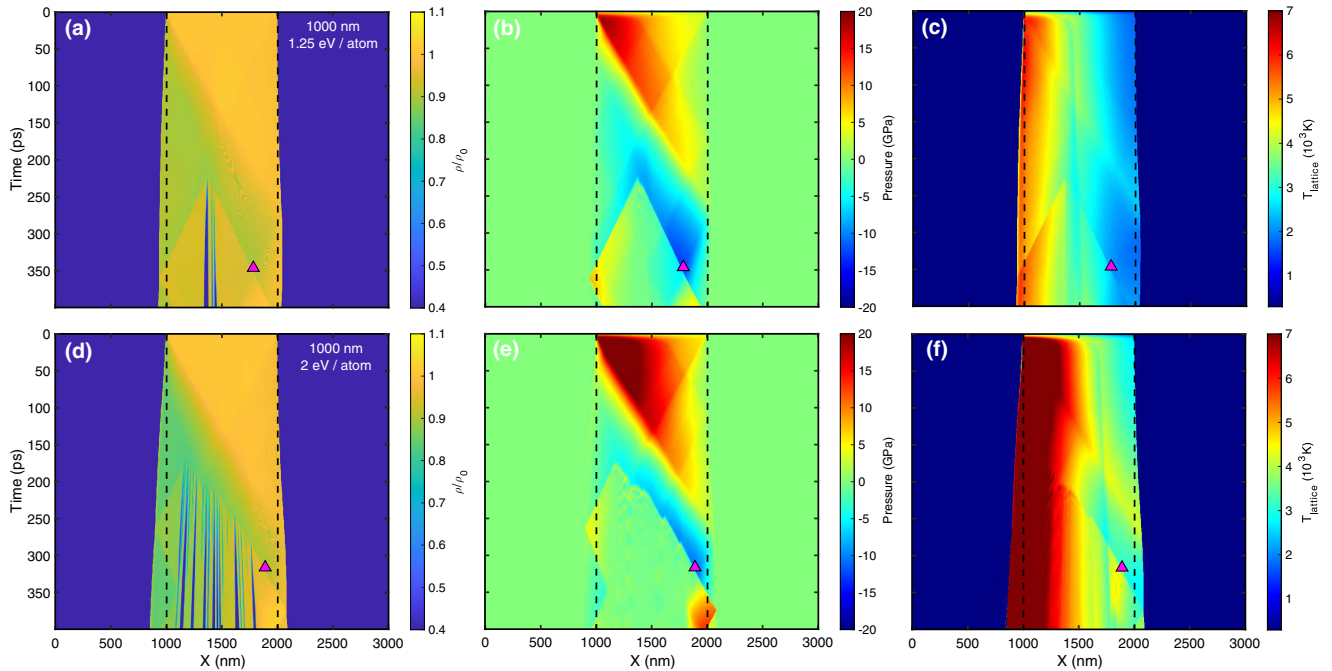


FIG. 10. Space-time plots of the density, pressure, and lattice temperature for a 1000-nm-thick freestanding tantalum foil. (a)–(c) correspond to average lattice heating to 1.25 eV/atom, while the heating is to 2 eV/atom in (d)–(f). In (d), the increased rate of void nucleation is evident. The dashed black lines in each panel indicate the initial foil boundaries and the purple triangles denote the position and time at which the tensile stress reaches its maximum magnitude. Comparing (a) and (b), it is clear that the void formation region is separate from the region of peak tensile stress as a result of thermal softening.

phase space trajectory reveals that even for the front surface of the foil, where the temperature is highest, the trajectory enters the vapor dome at a temperature of 10^4 K, well below the critical point.

Finally, the spatial profile of the hydrodynamic pressure is plotted in Fig. 11 for selected times within the simulation.

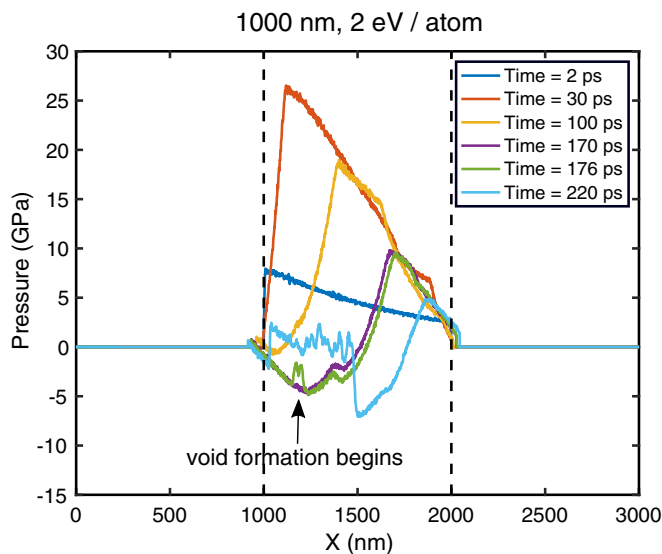


FIG. 11. Line out of the hydrodynamic pressure at selected times, from a simulation with a 1000-nm-thick freestanding tantalum foil heated to 2 eV/atom. The black arrow indicates the position of the first void, which appears in the simulation at 180 ps.

This plot highlights the presence of the extreme thermal and stress gradients across the 1000-nm-thick foil. Between the times of 2 ps and 30 ps, the foil continues to heat due to the slow transfer of energy from the electrons to the lattice. It is also clear that stress confinement occurs over a large volume of the foil, with only a small degree of pressure release from the irradiated surface at 30 ps. The tension on the irradiated side of the foil exceeds the tensile strength of the material around 170 ps, subsequently followed by void formation as indicated by the black arrow. This profile is demonstrably different to that of the 300-nm foil, presented in Fig. 7. For the 1000-nm foil, we see void formation begins close to the irradiated surface and propagates into the bulk, where the magnitude of tensile stress is greater. At 220 ps, we can see the tension is still increasing in magnitude toward the rear of the foil. This demonstrates the important role thermal softening plays for the thick foil, whereas for the 300-nm foil in Fig. 7 the magnitude of the peak tensile stress coincides with the void formation region.

V. DISCUSSION

The aim of this paper is to determine the cavitation threshold and subsequent ablation dynamics for tantalum foils over a range of thickness values. We report that the cavitation threshold for the 150-nm foil is 2 eV/atom, which is higher than that of thicker foils. As the foil thickness increases to ≥ 300 nm, the behavior becomes consistent and we observe the cavitation threshold at 1.25 eV/atom, independently of the foil thickness. In all simulations, we confirm that destruction of the foil results from cavitation and subsequent ablation,

indicating that damage is mechanical in nature over the range of incident x-ray energies investigated. Evidence of cavitation is presented in the form of space-time plots, which show the formation and growth of voids coincident with regions where the magnitude of tensile stress is large. Additional analysis of the trajectory the foils follow through (density-temperature) phase space shows the subsequent stages of isochoric heating across the melt curve, followed by a transition across the coexistence line into the vapor dome where cavitation is increasingly likely.

To further rule out the presence of explosive boiling in the simulations, the upstream free surfaces of the foils were analyzed, which are subjected to the highest temperatures in the sample. Despite the extreme temperatures (the free surface reaches 10 300 K for the 1000-nm foil heated to 2 eV/atom), we observed no signatures of vaporization. We report no surface removal of atoms or void formation within the first 100 nm of the foil, for any conditions studied, up to several hundred ps after irradiation. The free surfaces remain well-defined and show free surface velocities (of the order several hundred ms^{-1}) consistent with those expected on the basis of hydrodynamic release of fully dense Ta [70]. The average thermodynamic trajectory of the material located within four units cells of the upstream free surface remains close to the liquid-vapor dome binodal due to the absence of tensile stress in this region. This is consistent with a lack of significant vaporization, indicating primarily mechanical ablation for the simulation parameters chosen in this study.

We now provide an overview of the simulation results, in terms of the maximum and minimum values of the hydrostatic pressure (P), and compare against existing studies. Figure 12(a) shows the peak pressure for each foil (denoted with a different color) as a function of the deposited energy, measured in eV/atom. It is important to note that, here, the position of the peak pressure varies with the foil thickness and the level of heating. For each thickness under consideration, the peak pressure increases linearly with the degree of heating. This behavior is expected, given that this reflects the increasing thermal pressure due to stress confinement over a larger region of the foil. As described in Ref. [25], the condition for stress confinement is that the duration of the radiation pulse and the electron-lattice equilibration time must be less than the timescale associated with thermal expansion (related to the speed of sound at ambient density). For the 150-nm foil, at the ablation threshold, the timescale associated with thermal expansion is approximately 40 ps. This is comparable to the electron-lattice equilibration time of 30 ps. As the foil thickness increases to 1000 nm, the thermal expansion timescale increases to approximately 227 ps, which is much greater than the equilibration time (which is still 30 ps). This means a larger volume of the foil is heated under the condition of stress confinement, resulting in higher thermal pressure.

In Fig. 12(b), the hydrostatic pressure at the time of maximum tension, which we refer to as the minimum pressure, is plotted for each foil thickness as a function of deposited energy. Again, the position of the measurement varies with the target thickness and level of heating. As the thickness increases, the peak tension shifts toward the rear of the foil due to thermal softening. As discussed, the magnitude of the minimum pressure is lower for the 150-nm foil (indicated by

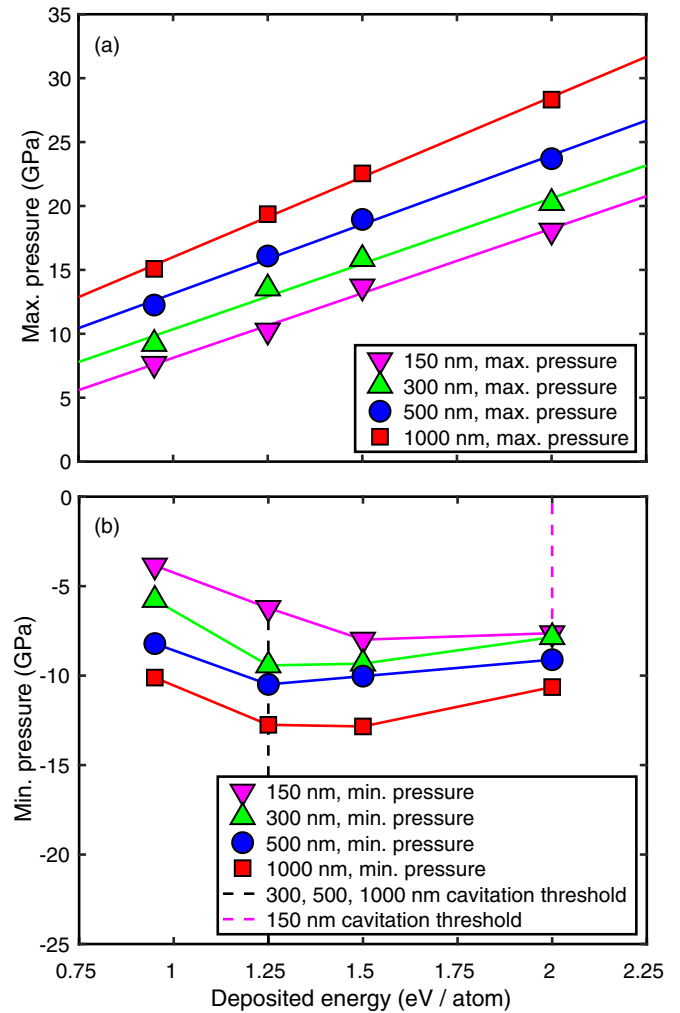


FIG. 12. Plots of the (a) maximum hydrostatic pressure and (b) the hydrodynamic pressure at the time of maximum tension (i.e., peak σ_{xx}) for different levels of lattice heating. Each color corresponds to a different foil thickness, with purple, green, blue, and red indicating foils of 150-, 300-, 500-, and 1000-nm thicknesses, respectively. The dashed purple line in (b) indicates the cavitation threshold for the 150-nm foil, while the dashed black line is the ablation threshold for the thicker foils.

the purple curve) due to poor stress confinement. Although thermal softening is present for all of the simulations, the pressure release in the 150-nm foil is insufficient to exceed the tensile strength of the material until the heating reaches 2 eV/atom. The magnitude of the minimum pressure reached in the 150-nm simulations therefore increases with deposited energy, indicating the release of a larger thermal pressure at the end of the isochoric heating stage. For the thicker foils (≥ 300 nm), the importance of thermal softening can be inferred from the shape of the curves in Fig. 12(b). At the lowest level of heating, to 0.95 eV/atom, thermal softening is insufficient to lead to failure of the foil. Since the tensile strength has not been exceeded, marginally increased magnitudes of minimum pressure can be withstood upon further heating. The cavitation threshold for each foil thickness is then located at the minimum of the corresponding curve in Fig. 12(b).

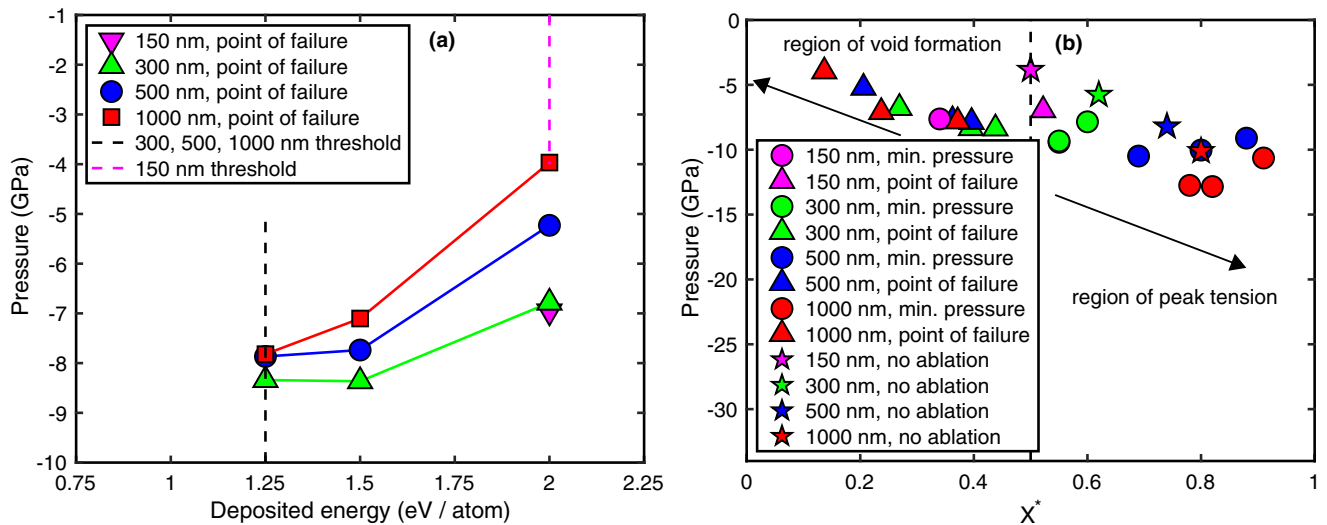


FIG. 13. (a) Pressure at the time of peak tension plotted as a function of the level of heating for different values of foil thickness. In contrast to Fig. 12, measurements are taken at the point of failure, i.e., the location of void formation closest to the irradiated side. As the level of heating increases, the magnitude of tension within the foil decreases. (b) Pressure at the time of maximum tension, plotted as a function of the normalized position within the foil. The colored triangles denote measurements at the point of failure and the colored circles indicate measurements taken at the location where the tension reaches its maximum magnitude. The colored stars indicate cases where no cavitation or ablation occurs, serving as references, while the vertical dashed line marks the center of the foil. (b) shows that, as the thickness increases, void formation occurs closer to the irradiated surface while the peak tension shifts toward the foil rear surface.

As the degree of heating increases, so does the magnitude of thermal softening, reducing the maximum tensile stress which can be supported within the foil. Note that the curve corresponding to the 150-nm foil follows the same trend as the thicker foils, given that the cavitation threshold is located at 2 eV/atom. It is expected that for further heating, the magnitude of the minimum pressure would decrease, as it does for thicker foils. It should also be noted that this behavior, in which the magnitude of the peak tensile stress increases with fluence up to the cavitation threshold before either saturating or decreasing, is in excellent agreement with the simulation results presented in Ref. [25] for nickel foils.

The hydrodynamic pressure values in Fig. 12(b) are measured at the location and time where the magnitude of tension reaches its maximum, which varies with foil thickness and level of heating. To obtain an estimate of the tensile strength of tantalum under extreme heating conditions, we must also determine the magnitude of tension at the point of failure. Such analysis also enables comparison against recent simulation [27] and experimental studies [39,71] investigating the tensile strength of warm dense tantalum, which will be detailed later. In Fig. 13(a), the minimum pressure value at the point of failure is plotted as a function of the level of heating for different foil thickness values (denoted by different colored markers). The point of failure in each simulation is the location of the void closest to the irradiated side of the foil. The simulations with a higher degree of heating exhibit multiple voids which could be used for the measurement but, for consistency, and to ensure we are reporting the maximum spatial separation of the void formation region from the region of peak tensile stress, we choose the void closest to the irradiated side. The measurement at the point of failure is made by analyzing the spatial pressure profile (such as those demonstrated in Figs. 7 and 11), taking

the value of pressure at the moment it begins to jump back toward zero, following void formation. Note that the data set is reduced compared to Fig. 12 as we only include simulations where the cavitation threshold has been exceeded. As the level of heating increases, the magnitude of the minimum pressure at the point of failure decreases. The effect becomes more pronounced as the foil thickness increases, due to the increasing thermal gradient, with failure occurring in the hot material on the side of irradiation. For example, for the 1000-nm foil, the minimum pressure at the point of failure decreases in magnitude from -7.82 GPa to -3.97 GPa, as the level of heating increases from 1.25 to 2 eV/atom.

The value of the pressure minimum is plotted as a function of the normalized position within the foil where each measurement is taken in Fig. 13(b). This normalized distance is defined as $X^* = (x_m - \ell)/\ell$, where x_m is the location of the measurement and ℓ is the target thickness. The measurements taken at the location where the tension reaches its maximum magnitude [i.e., the same data points which appear in Fig. 12(b)] are denoted with colored circles, with different colors representing different target thickness values. In contrast, the colored triangles indicate measurements at the point of failure.

The stars correspond to the pressure (at the time of maximum tension) from simulations where no cavitation or ablation occurs, which act as a reference for each value of target thickness. For the 150-nm foil, the uniform heating means the rarefaction waves from the free surfaces overlap at the center of the foil. As expected, the peak tension occurs at a value $X^* = 0.5$, indicated by the purple star. As the thickness increases, the asymmetry in the heating means the peak tension occurs deeper within the foil, at values of X^* tending toward unity.

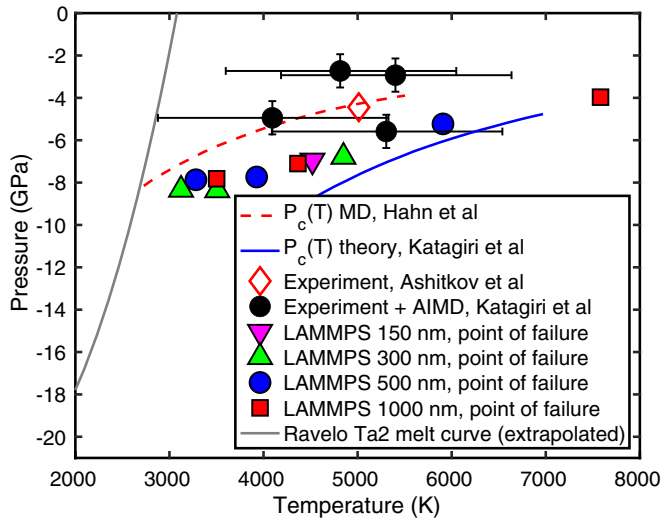


FIG. 14. Demonstration of the thermal softening effect by which the magnitude of the tensile stress within the foil is reduced upon heating. Each measurement is taken at the point of failure, i.e., at the location of void formation closest to the side of irradiation. The purple, green, blue, and red markers correspond to data points in this investigation, with each color denoting a different target thickness. We compare against the results of quasi-isentropic compression and tension simulations in Hahn *et al.* [27], indicated by the dashed orange line. We also compare the data points to the experimental and AIMD data presented in Katagiri *et al.* [39], represented by the black circles with associated error bars. Following Ref. [39], we also include a data point from the laser ablation experiment of Ashitkov *et al.* [71], and the prediction of nucleation theory, denoted by the solid blue curve, plotted using data from Ref. [39]. The grey curve is the melt curve for the Ravelo Ta2 potential [31], extrapolated to negative pressures using the fitting equation presented in Ref. [50] and converted to density-temperature space using the EoS spreadsheet in Ref. [51].

The key point of Fig. 13(b) is that, as the target thickness increases, the separation of the void formation region and the region of peak tensile stress also increases. This is evinced by the greater distance between the clusters of triangular and circular markers for each target thickness. Furthermore, Fig. 13(b) acts as a means of translating between Fig. 12(b), which shows the minimum pressure as a function of the level of heating, regardless of the location within the foil, and Fig. 13(a), where the minimum pressure is plotted as a function of heating, as measured at the point of failure.

The thermal softening effect is investigated in more detail in Fig. 14. The colored markers denote data points from this investigation, with each color corresponding to a different target thickness. These data points are compared to the results of MD simulations investigating quasi-isentropic (QI) compression and tension of tantalum in Hahn *et al.* [27], denoted with a dashed orange curve. The QI method is employed to replicate the conditions of shock compression and release experiments, with the advantage that such simulations can provide homogeneous compression and stretching across the sample at a fixed strain rate. The simulations in Ref. [27] are found to be in excellent agreement with the results of the laser ablation experiment (using an optical laser pulse)

in Ashitkov *et al.* [71], as indicated by the orange diamond. We further relate our results to the experimental and *ab initio* MD (AIMD) data points presented in Katagiri *et al.* [39], denoted by black circles with corresponding error bars. While Ref. [39] is not strictly a laser ablation experiment, it does report on the formation of tension within liquid tantalum during a hydrodynamic compression and release experiment and predicts the scaling of the magnitude of tension as a function of temperature, which is also an aim of this paper. The grey curve in Fig. 14 is the EAM potential melt curve, extrapolated to negative pressures. All our data points sit above the melt curve, again indicating that the foil must first melt before failure can occur via cavitation. Finally, we include the predictions of classical nucleation theory. This is plotted with a solid blue curve in Fig. 14 using data from Ref. [39].

Figure 14 demonstrates that the trend in our data is in agreement with Ref. [27]. The QI compression and tension in those simulations is performed at a constant strain rate of $\dot{\epsilon} = 10^9 \text{ s}^{-1}$. Estimation of the peak strain rate from our simulations predicts values in the range $\dot{\epsilon} \approx 1-3 \times 10^9 \text{ s}^{-1}$, depending on the thickness and level of heating, hence we expect the ablation dynamics to be similar, given we are probing a similar region in strain-rate space. We note that the magnitude of tension is somewhat higher in this paper compared to the data in Ref. [27]. This could be due to the choice of potential, as Ref. [27] uses the Ravelo Ta1 potential [31], which has slightly different thermal properties (such as underestimating the thermal expansion coefficient to a greater degree than the Ta2 potential). Another consideration is that the QI compression and tension in Ref. [27] leads to a high density of dislocations, which is predicted to reduce the tensile strength of the material, which may again explain the higher magnitudes of tension in our investigation.

We also find agreement with Ref. [39], whose data points also sit somewhere between the simulations of Ref. [27] and the predictions of classical nucleation theory. Similarly to Ref. [39], our data points sit above the curve predicted by classical nucleation theory. This discrepancy could be caused by anisotropy during the pressure release, as highlighted in Ref. [39]. The agreement between the data sets in Fig. 14 indicates that our simulations are probing a similar region of P - T space as the aforementioned experiment. It is reasonable then that TTM-MD simulations may be used as a means of interpreting the results of hydrodynamic compression and release experiments, and understanding the underlying physics on timescales which the experiment cannot probe (i.e., fs resolution of the temperature evolution and ps resolution of atomic trajectories).

It is important to state that we are reporting agreement between the results of TTM-MD simulations (this paper), MD simulations of QI compression and tension (Ref. [27]), and experimental and AIMD data points from a hydrodynamic experiment (Ref. [39]). This agreement suggests an equivalence between hydrodynamic compression and release experiments and isochoric heating experiments.

This result has implications for the interpretation of existing experiments and in guiding future studies. The relevance to hydrodynamic experiments probing liquid tantalum states has already been discussed, but the simulations can also improve understanding of investigations into the tensile strength

of solid tantalum. For example, the spall strength of tantalum is investigated experimentally in Ref. [72] and supported by large-scale MD simulations. In those simulations, a piston is launched into the sample to recreate conditions of hydrodynamic compression and release. The temperatures are likely much lower in Ref. [72] compared to our investigation, given that failure occurs in the solid state. However, the reported spall strength of ≈ 15 GPa from a 3950-nm-thick sample in Ref. [72] is comparable to the values of tension in our paper, for thick foils heated to below the threshold for cavitation [for example, see the values of the minimum pressure for the 1000-nm foil in Fig. 12(b)]. Although there appears to be agreement between the experiment and simulations at low temperatures, the TTM-MD simulations provide a means of probing the tensile strength of materials at extreme temperatures, perhaps even outside the P - T regime currently accessible at XFELs.

VI. CONCLUSIONS

Much prior research into the behavior of tantalum at extreme conditions has focused on computational investigations of its tensile properties [27,31,73], such as the spall strength and stress-induced phase transitions [30]. Given that facilities are now capable of delivering exceptionally bright pulses of high-energy x-rays, there is a desire to investigate the ablation processes which underpin the destruction of (micron) thick tantalum foils under high-energy x-ray irradiation. While these mechanisms remain poorly understood within the high-energy x-ray regime, progress in understanding ablation under optical and soft x-ray pulses has historically been facilitated by computer simulations. Specifically, these simulations employ hybrid two-temperature MD codes, which are capable of describing the ablation process on the atomic scale and on ps timeframes.

In this paper, the cavitation threshold and ablation dynamics are investigated for a range of tantalum foil thicknesses and under different levels of heating. The x-ray energies vary in the range 1–5 keV, which is at the lower end of the operating energy range of current XFEL facilities. We reiterate that stress confinement occurs over a small volume for the thin (150-nm-thick) foil, resulting in a lower thermal pressure, and a smaller magnitude of tension upon release of this stress confined state. The cavitation threshold for this case is 2 eV/atom, which is greater than that of thicker foils. As the thickness increases to ≥ 300 nm, we report a cavitation threshold of 1.25 eV/atom, which is independent of the foil thickness. These results are supported by the experimental findings in McHardy *et al.* [74], in which tantalum foils irradiated at the EuXFEL (at an energy of 17.8 keV) exhibit damage patterns consistent with the ejection of liquid material from the laser spot, and clear shearing of the foils suggests tensile stress plays a role in the ablation process.

This current paper aims to elucidate the timescale over which x-ray energy is coupled into the electrons and the lattice immediately following irradiation, and to determine the damage mechanism. In this respect, we find that electron-lattice equilibration occurs over a timescale of approximately 30 ps, and damage occurs due to cavitation and subsequent ablation. The results of this paper are timely in that they extend TTM-MD simulations into the regime of high energy

x-rays, assisting in the interpretation of experimental results. Improved understanding of the underlying mechanisms of energy transfer and ablation during high energy x-ray irradiation may lead to applications including microstructuring of material surfaces and development of beamline optics for free-electron lasers.

Finally, we note some limitations of the current investigation. As previously stated, the upper limit of the incident x-ray energy is restricted to 5 keV. This is within the operating range of XFEL facilities and can still be used to describe the behavior observed in in XFEL experiments. However, the delivered x-ray energy is lower than the 17.8 keV typically delivered by the EuXFEL. The restriction arises because, as the x-ray energy increases, ballistic electrons are expected to play a more important role in the interaction. More precise modeling of these ballistic electrons, in terms of their energy distribution and mean-free path, is needed before these can be implemented in the TTM-MD simulations. It is also worth noting that the simulations do not consider ionization processes or account for plasma behavior, which are important at higher fluences. Follow-up work should address these limitations, possibly by using Monte Carlo simulations to predict the ballistic electron range. We also note that the electron thermal conductivity chosen in this study is likely an underestimate of the true value, however, progress in this respect will involve turning to DFT calculations to predict the functional form of the electron thermal conductivity with temperature, and modifying the simulation source code to incorporate this. We also note that we have used idealized tantalum crystals in this investigation, constructed from a regular bcc lattice. Under experimental conditions, it is often necessary to consider the role of defects in the crystal lattice, which may influence its mechanical properties. Future work may address the role of defects on the determination of the ablation threshold in more detail, however, we direct the interested reader to Refs. [27,50,75,76], where the spall strength of tantalum has already been investigated as a function of grain size and strain rate.

ACKNOWLEDGMENTS

This work was supported by Grants No. EP/S022155/1, No. EP/S025065/1, and No. EP/P024513/1 from the UK Engineering and Physical Sciences Research Council (EPSRC), and made use of resources provided by the Edinburgh Compute and Data Facility (ECDF). This result is part of a project that has received funding from the European Research Council (ERC) under the European Union's Horizon 2020 research and innovation program (Grant Agreement No. 101002868). P.G.H. and A.D'S. are grateful for support from AWE via OxCHEDS (the Oxford Centre for High Energy Density Science), and J.D.M. is grateful for support from AWE via a CASE studentship. The authors would also like to thank A. Higginbotham for valuable discussions.

APPENDIX

1. Mixed phase simulations

Mixed phase simulations were performed to determine the vapor dome boundaries for the Ravelo Ta2 potential [31] used

in this study. The simulation scheme involves first heating a tantalum lattice to a target temperature in the range 8×10^3 – 17×10^3 K. The system is given time to evolve with the positions and velocities sampled from the isothermal-isobaric (number, pressure and temperature, or NPT) ensemble, with a target pressure of zero bar over a typical timescale of 50 ps. This generates a stable sample of molten tantalum. The simulation box is then resized to accommodate regions of vacuum on either side of the (molten) liquid sample, into which atoms of the gaseous phase can evaporate. The system is given a further 50 ps for the vapor to saturate, then the liquid and vapor phases evolve according to a NVT (number, volume, temperature) thermostat until a stable state is reached. This stable state is defined as one in which the temperatures in the liquid and vapor phases differ by no more than 50 K, and the vapor density does not vary by more than 1% in a 25-ps period. For the system to properly thermalize, we impose the condition that the size of the vacuum region (and therefore of the vapor phase) must be greater than the mean-free path of an atom in the vapor phase. Note that the requirement that the vapor phase reaches a stable state restrains the range of temperatures over which the mixed phase simulations can be employed. Below a temperature of 8×10^3 K, the typical collision time between atoms exceeds 500 ps, making it unlikely that the liquid and vapor will reach thermodynamic equilibrium over the timescales accessible in molecular dynamics simulations. We also note that in the case where the saturated vapor phase contains fewer than 1000 atoms, the dimensions of the simulation box are expanded to accommodate more atoms of this phase, and the system is given time to relax to a stable state under the NVT thermostat, as described above. These steps (evaporation and relaxation) are iterated until a sufficient number of atoms exist in the vapor phase.

After reaching equilibrium, the average density profile is constructed by sampling the system at regular intervals over a timescale of 250 ps. Given a sufficient number of atoms in the initial tantalum lattice, the liquid region remains stable and a clear distinction between the liquid and vapor regions is observed (albeit separated by a thin transition layer). The density spatial profile is then fitted with a hyperbolic tangent function, giving the density of the liquid and vapor phases at the target temperature. Repeating this simulation scheme over a range of target temperatures enables the boundary of the vapor dome to be mapped out. The phase boundaries obtained from the mixed phase simulations are plotted in Fig. 1, where the dotted blue and orange curves are obtained by fitting the simulation data points to the following equations (adapted from Ref. [48]):

$$\rho_{\text{vapor}} = \rho_{\text{diam}} - \rho_{\text{diff}}, \quad (\text{A1})$$

$$\rho_{\text{liquid}} = \rho_{\text{diam}} + \rho_{\text{diff}}, \quad (\text{A2})$$

where

$$\rho_{\text{diam}} = \rho_c \left(1 + a(T_c - T) + c(T_c - T)^{\frac{2}{3}} \right), \quad (\text{A3})$$

$$\rho_{\text{diff}} = b(T_c - T)^{\frac{1}{3}} \left(1 + b_2(T_c - T)^{\frac{2}{3}} \right), \quad (\text{A4})$$

with $T_c = 17.3 \times 10^3$ K and $\rho_c = 3.64 \text{ g cm}^{-3}$ denoting the critical temperature and density, respectively, and the remaining fitting parameters detailed below:

$$a = -5.12 \times 10^{-5} \text{ K}^{-1}, \quad (\text{A5})$$

$$b = 0.384 \text{ g cm}^{-3} \text{ K}^{-1/3}, \quad (\text{A6})$$

$$b_2 = -2.77 \times 10^{-4} \text{ K}^{-2/3} \quad (\text{A7})$$

$$c = 0.00320 \text{ K}^{-2/3}. \quad (\text{A8})$$

Comparing the mixed phase simulation results to the phase boundaries reported by Leitner *et al.* (denoted by the solid blue and orange curves in Fig. 1), it is clear that the mixed phase data points sit at higher temperatures and predict a higher critical temperature. This discrepancy could be explained by the fact that the Ravelo Ta2 potential underestimates the Grüneisen parameter at ambient conditions by approximately 40% (as reported in Ref. [33]), which subsequently results in an underestimate of the thermal expansion coefficient of tantalum. For a given temperature, we would then expect the simulations to predict a higher density than the experimentally measured value, which is indeed the case. A potential consequence of this higher critical temperature compared to the experimental measurement is that the simulations will overestimate the threshold for high fluence ablation mechanisms. While this is, again, a limitation imposed on the study by the choice of potential, we reiterate that it is extremely difficult to find a potential which faithfully encapsulates all the physical processes leading to ablation. Given the demonstrable ability of the Ravelo Ta2 potential to recreate the melt curve of tantalum and its robustness in the high pressure regime, we believe this is a suitable choice.

2. Estimating the critical void radius

The critical void size is estimated using a configuration similar to that of the mixed-phase simulations. The steps are as follows:

(1) A tantalum slab is heated to 12×10^3 K under a NPT barostat with a target pressure of zero bar for 60 ps.

(2) The liquid slab is subjected to isotropic tension at a strain rate of $6 \times 10^{-3} \text{ s}^{-1}$ for 250 ps.

(3) The dimensions of the simulation box are increased to create vacuum regions into which the vapor phase can evaporate over a period of 50 ps.

(4) The system is given a further 800 ps for the vapor phase to stabilize (in terms of number density).

(5) Averages of the density spatial profile are obtained at regular intervals over a timescale of 25 ps.

Following the approach described in Ref. [43] using classical nucleation theory, the parameters which are required to estimate the critical void size are the width of the transition region between the liquid and vapor phases (denoted δ) and the value of surface tension across a planar interface of liquid and vapor (denoted γ_0). Fitting a hyperbolic tangent function to the average density profile yields a value of 2.07 \AA for the width of the liquid-vapor interface. As described in Ref. [43], this width can be used to approximate the characteristic length in the so-called Tolman equation, relating the size of the voids to the values of tension across the interface. The above

estimate of the Tolman length is in excellent agreement with the prediction of the liquid drop model in Ref. [77].

The surface tension is evaluated using the method described in Ref. [78], where the spatial profile of the differential stress (the difference between the normal and tangential components of the stress tensor) is integrated across the interface. This yields $\gamma_0 = 0.4479 \text{ Jm}^{-2}$. This is greater than the value obtained via scaling of the surface tension with temperature reported in Ref. [79], which predicts a value of 0.3 Jm^{-2} when extrapolated to a temperature of $12 \times 10^3 \text{ K}$. It is also higher than the value of 0.22 Jm^{-2} predicted by DFT in Ref. [80]. The discrepancy may be related to the fact the potential underestimates the thermal expansion coefficient, resulting in higher density (and surface tension) at a given temperature compared to experimental measurements.

The critical void radius is then calculated from Eq. (A9) below [43]:

$$\frac{1 + \frac{3\delta}{r_c} r_0^*}{\left(1 + \frac{2\delta}{r_c}\right)^2 r_c} = 1. \quad (\text{A9})$$

The quantity $r_0^* = 2\gamma_0/|P|$ is estimated using the maximum magnitude of tension in the simulation, which is 1.33 GPa. Substituting δ and γ_0 into Eq. (A9) yields a critical void radius of $r_c = 4.03 \text{ \AA}$. This value is much smaller than the transverse dimensions of the simulation box, giving confidence that the growth of critically sized voids is not restrained by the simulation dimensions and therefore that the cavitation threshold is correctly reported.

3. Synthetic x-ray diffraction data

In this paper, we demonstrate that under hard x-ray irradiation, ablation occurs in freestanding tantalum foils upon heating to 1.25 eV/atom. The ablation mechanism, over the range of fluence investigated, is cavitation, where the tension within the molten foil exceeds the material tensile strength. The primary diagnostic for determining that the metal is molten is by identifying regions within the foil where the lattice temperature exceeds the melting point of the EAM potential used in this study. It is possible to corroborate this result using synthetic XRD from the TTM-MD simulations, as presented in this section.

Synthetic XRD patterns are obtained from the simulations using the custom USER-DIFFRACTION package in LAMMPS, described in detail in Refs. [81,82]. The XRD calculation can be performed in postprocessing by loading in atomic positions from a standard dump file. This allows flexibility for the user to vary the wavelength of the incident x-ray radiation, as well as changing the region of interest and the time at which it is probed. The computational cost of the algorithm is reduced by specifying the angular range of interest. In the proceeding analysis, the XRD patterns are obtained for diffraction angles in the range $2\theta = 20\text{--}55^\circ$, which captures reflections from the tantalum (110), (200), (211), and (220) Miller planes.

Synthetic XRD patterns are presented for the 150-nm-thick foil, heated to 2 eV/atom, in Fig. 15. The top and bottom panels correspond to diffraction data from the upstream free surface and center of the foil, respectively. In each case,

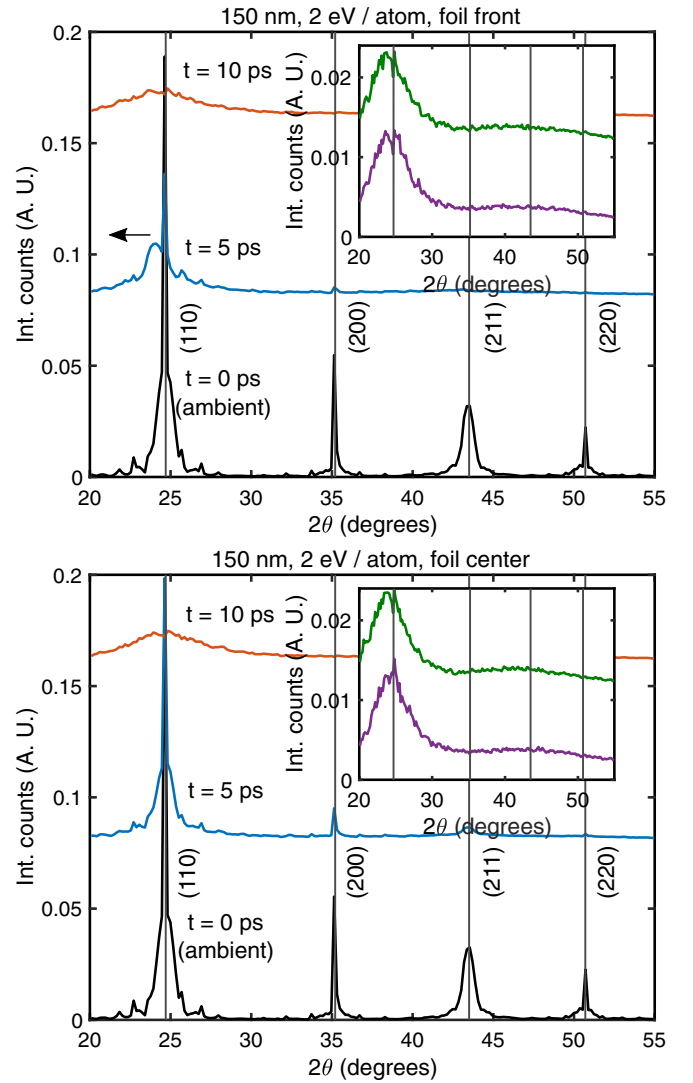


FIG. 15. Synthetic x-ray diffraction patterns from simulations with a 150-nm-thick foil, heated to 2 eV/atom. The top panel shows diffraction patterns obtained from a volume of $15 \times 15 \times 15$ unit cells located at the foil front surface, while the bottom panel shows diffraction from a region of similar volume, this time located at the center of the foil (which remains under stress confinement conditions for longer). In both panels, the black pattern corresponds to the diffraction pattern from a tantalum crystal at ambient conditions (after equilibration to 300 K), while the blue and orange patterns are obtained at 5 and 10 ps, respectively. At the front of the foil, the (110) Bragg peak is shifted from the ambient position, at a time of 5 ps, due to tension. The insets show the diffraction patterns taken at 30 and 50 ps (purple and green profiles, respectively), with a rescaled vertical axis to emphasize the broad liquid peaks. The vertical lines indicate the location of the diffraction peaks from the Miller planes labeled with (h,k,l) indices at the bottom of each line. The panels show that the lattice has melted by 30 ps, with the sharp peaks replaced by broad liquid peaks.

the black pattern corresponds to diffraction from tantalum at ambient conditions (taken after the crystal has been equilibrated to 300 K), showing peaks at the angles associated

with the labeled Miller planes. The blue and orange lines indicate the XRD patterns at 5 and 10 ps, respectively. The peaks corresponding to the (110), (200), and (211) planes are still present at 5 ps, however, these peaks decrease in intensity and become broad and liquidlike at 10 ps. At the front of the foil, at a time of 5 ps, the location of the (110) Bragg peak is shifted from the ambient position due to tension. The insets in each panel show the XRD patterns at 30 and 50 ps (after the cutoff time of the TTM module), with a rescaled vertical axis to provide a clearer view of the broad, liquidlike peaks associated with molten material. The synthetic XRD profiles compliment the space-time plot of the lattice temperature in Fig. 4(f), demonstrating that the front and center of the foil undergo melting upon heating to 2 eV/atom.

4. Convergence testing of the TTM-MD simulations

It is known that the ablation dynamics have a dependence on the size of the simulation cross section [68]. There are two constraints on the cross-sectional dimensions of the presented simulations. The first is that the cross section must be greater than the diameter of a critically sized void to avoid incorrectly reporting the ablation threshold. This condition is indeed met in the simulations, given that the cross section is 19.8 nm and the size of the critical void is ≈ 4 Å.

As reported in Ref. [68], there is an additional consideration in the case of periodic boundary conditions. If the cross section is too small, then voids can interact with their mirror image across the periodic boundary, resulting in tensile stress with an artificially high magnitude. To check this is not the case in the current study, convergence tests were conducted by running the 300-nm simulations with different transverse dimensions. The cross sections were 15×15 , 30×30 , and 60×60 unit cells, and for each case the value of the hydrostatic pressure at the time of maximum tensile stress was recorded. Note that it was impractical to increase the cross section beyond 60×60 unit cells (corresponding to

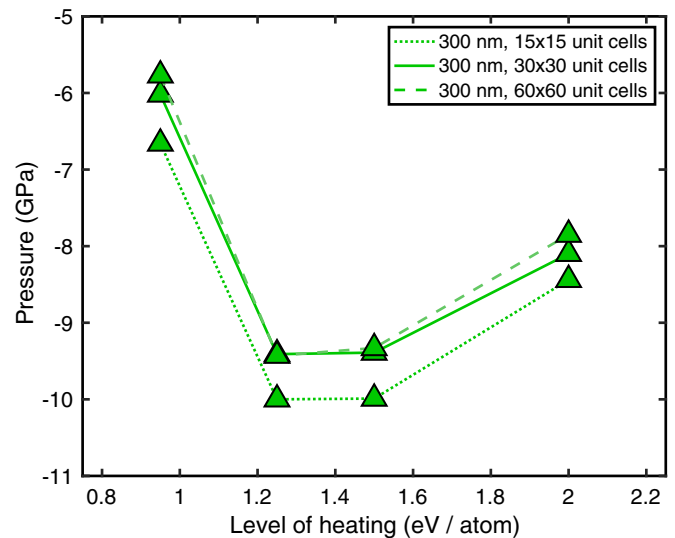


FIG. 16. Pressure at the time of maximum tension, presented as a function of the level of heating for the 300 nm simulations. Different transverse dimensions are tested to determine the simulation size necessary to prevent overestimation of the tensile stress.

6 544 800 atoms for the 300-nm case) due to the required run time of the simulations.

The results of the convergence testing are presented in Fig. 16. Comparing the 15×15 and 30×30 unit cell simulations, the magnitude of the tensile stress at the ablation threshold is 6.3% greater in the simulation with the smaller dimensions. In contrast, the magnitude of the stress reported in the 30×30 and 60×60 unit cell simulations at the ablation threshold differ by only 0.2%. The simulations presented in this paper, with cross-sectional size of 60×60 unit cells, are therefore sufficiently large to prevent overestimation of the magnitude of tensile stress.

- [1] G. Norman, S. Starikov, V. Stegailov, V. Fortov, I. Skobelev, T. Pikuz, A. Faenov, S. Tamotsu, Y. Kato, M. Ishino *et al.*, Nanomodification of gold surface by picosecond soft x-ray laser pulse, *J. Appl. Phys.* **112**, 013104 (2012).
- [2] Y. Rosandi and H. M. Urbassek, Ablation of a nanostructured metal surface by ultrashort x-ray pulses, *Appl. Surf. Sci.* **307**, 142 (2014).
- [3] M. Nishikino, N. Hasegawa, T. Tomita, Y. Minami, T. Eyama, N. Kakimoto, R. Izutsu, M. Baba, T. Kawachi, and T. Suemoto, Formation of x-ray Newton's rings from nano-scale spallation shells of metals in laser ablation, *AIP Adv.* **7**, 015311 (2017).
- [4] M. Ishino, N. A. Inogamov, S. Tamotsu, V. V. Zhakhovsky, N. Hasegawa, I. Y. Skobelev, A. Y. Faenov, T. A. Pikuz, K. Mikami, T. Kawachi *et al.*, Study of damage structure formation on aluminum film targets by picosecond soft x-ray laser ablation around threshold region, *Appl. Phys. A* **124**, 649 (2018).
- [5] J. Chalupský, L. Juha, J. Kuba, J. Cihelka, V. Hájková, S. Koptyaev, J. Krása, A. Velyhan, M. Bergh, C. Coleman *et al.*, Characteristics of focused soft x-ray free-electron laser beam determined by ablation of organic molecular solids, *Opt. Express* **15**, 6036 (2007).
- [6] J. Chalupský, L. Juha, V. Hájková, J. Cihelka, L. Vyšíň, J. Gautier, J. Hajdu, S. Hau-Riege, M. Jurek, J. Krzywinski *et al.*, Non-thermal desorption/ablation of molecular solids induced by ultra-short soft x-ray pulses, *Opt. Express* **17**, 208 (2009).
- [7] A. Nelson, S. Toleikis, H. Chapman, S. Bajt, J. Krzywinski, J. Chalupsky, L. Juha, J. Cihelka, V. Hajkova, L. Vysin *et al.*, Soft x-ray free electron laser microfocus for exploring matter under extreme conditions, *Opt. Express* **17**, 18271 (2009).
- [8] J. Chalupský, J. Krzywinski, L. Juha, V. Hájková, J. Cihelka, T. Burian, L. Vyšíň, J. Gaudin, A. Gleeson, M. Jurek *et al.*, Spot size characterization of focused non-gaussian x-ray laser beams, *Opt. Express* **18**, 27836 (2010).
- [9] J. Chalupský, T. Burian, V. Hájková, L. Juha, T. Polcar, J. Gaudin, M. Nagasono, R. Sobierajski, M. Yabashi, and J. Krzywinski, Fluence scan: An unexplored property of a laser beam, *Opt. Express* **21**, 26363 (2013).

- [10] J. Chalupský, P. Boháček, T. Burian, V. Hájková, S. P. Hau-Riege, P. A. Heimann, L. Juha, M. Messerschmidt, S. P. Moeller, B. Nagler, M. Rowen, W. F. Schlotter, M. L. Swiggers, J. J. Turner, and J. Krzywinski, Imprinting a Focused X-Ray Laser Beam to Measure Its Full Spatial Characteristics, *Phys. Rev. Appl.* **4**, 014004 (2015).
- [11] S. Nolte, C. Momma, H. Jacobs, A. Tünnermann, B. N. Chichkov, B. Welleghausen, and H. Welling, Ablation of metals by ultrashort laser pulses, *J. Opt. Soc. Am. B* **14**, 2716 (1997).
- [12] A. Semerok, C. Chaléard, V. Detalle, J.-L. Lacour, P. Mauchien, P. Meynadier, C. Nouvellon, B. Sallé, P. Palianov, M. Perdrix *et al.*, Experimental investigations of laser ablation efficiency of pure metals with femto, pico and nanosecond pulses, *Appl. Surf. Sci.* **138-139**, 311 (1999).
- [13] J. Kim and S. Na, Metal thin film ablation with femtosecond pulsed laser, *Opt. Laser Technol.* **39**, 1443 (2007).
- [14] K. Furusawa, K. Takahashi, H. Kumagai, K. Midorikawa, and M. Obara, Ablation characteristics of Au, Ag, and Cu metals using a femtosecond titanium sapphire laser, *Appl. Phys. A* **69**, S359 (1999).
- [15] M. Shirk and P. Molian, A review of ultrashort pulsed laser ablation of materials, *J. Laser Appl.* **10**, 18 (1998).
- [16] S. P. Hau-Riege, *High-Intensity X-rays–Interaction with Matter: Processes in Plasmas, Clusters, Molecules and Solids* (Wiley-VCH, Weinheim, 2011).
- [17] J. Reif, Basic physics of femtosecond laser ablation, in *Laser-Surface Interactions for New Materials Production*, Springer Series in Materials Science, Vol. 130, edited by A. Miotello and P. Ossi (Springer, Berlin, Heidelberg, 2010), pp. 19–41.
- [18] D. S. Ivanov and L. V. Zhigilei, Combined atomistic-continuum modeling of short-pulse laser melting and disintegration of metal films, *Phys. Rev. B* **68**, 064114 (2003).
- [19] B. J. Demaske, V. V. Zhakhovsky, N. A. Inogamov, and I. I. Oleynik, Ablation and spallation of gold films irradiated by ultrashort laser pulses, *Phys. Rev. B* **82**, 064113 (2010).
- [20] S. V. Starikov, V. V. Stegailov, G. Norman, V. E. Fortov, M. Ishino, M. Tanaka, N. Hasegawa, M. Nishikino, T. Ohba, T. Kaihori *et al.*, Laser ablation of gold: Experiment and atomistic simulation, *JETP Lett.* **93**, 642 (2011).
- [21] S. Starikov, A. Y. Faenov, T. Pikuz, I. Y. Skobelev, V. Fortov, S. Tamotsu, M. Ishino, M. Tanaka, N. Hasegawa, M. Nishikino *et al.*, Soft picosecond x-ray laser nanomodification of gold and aluminum surfaces, *Appl. Phys. B* **116**, 1005 (2014).
- [22] Y. Shen, Y. Gan, W. Qi, Y. Shen, and Z. Chen, Effect of the hot electron blast force on ultrafast laser ablation of nickel thin film, *Appl. Opt.* **54**, 1737 (2015).
- [23] S. V. Starikov and V. V. Pisarev, Atomistic simulation of laser-pulse surface modification: Predictions of models with various length and timescales, *J. Appl. Phys.* **117**, 135901 (2015).
- [24] Q. Zeng and J. Dai, Structural transition dynamics of the formation of warm dense gold: From an atomic scale view, *Science China Physics, Mechanics & Astronomy* **63**, 263011 (2020).
- [25] E. Leveugle, D. S. Ivanov, and L. V. Zhigilei, Photomechanical spallation of molecular and metal targets: Molecular dynamics study, *Appl. Phys. A* **79**, 1643 (2004).
- [26] L. Thomsen, Weak elastic anisotropy, *Geophysics* **51**, 1954 (1986).
- [27] E. N. Hahn, T. C. Germann, R. Ravelo, J. E. Hammerberg, and M. A. Meyers, On the ultimate tensile strength of tantalum, *Acta Mater.* **126**, 313 (2017).
- [28] D. Duffy and A. Rutherford, Including the effects of electronic stopping and electron–ion interactions in radiation damage simulations, *J. Phys.: Condens. Matter* **19**, 016207 (2007).
- [29] A. Rutherford and D. Duffy, The effect of electron–ion interactions on radiation damage simulations, *J. Phys.: Condens. Matter* **19**, 496201 (2007).
- [30] Z. Pan, Y. Li, and Q. Wei, Tensile properties of nanocrystalline tantalum from molecular dynamics simulations, *Acta Mater.* **56**, 3470 (2008).
- [31] R. Ravelo, T. C. Germann, O. Guerrero, Q. An, and B. L. Holian, Shock-induced plasticity in tantalum single crystals: Interatomic potentials and large-scale molecular-dynamics simulations, *Phys. Rev. B* **88**, 134101 (2013).
- [32] D. Tramontina, P. Erhart, T. Germann, J. Hawreliak, A. Higginbotham, N. Park, R. Ravelo, A. Stukowski, M. Suggit, Y. Tang *et al.*, Molecular dynamics simulations of shock-induced plasticity in tantalum, *High Energy Density Phys.* **10**, 9 (2014).
- [33] P. G. Heighway, M. Sliwa, D. McGonegle, C. Wehrenberg, C. A. Bolme, J. Eggert, A. Higginbotham, A. Lazicki, H. J. Lee, B. Nagler, H. S. Park, R. E. Rudd, R. F. Smith, M. J. Suggit, D. Swift, F. Tavella, B. A. Remington, and J. S. Wark, Nonisentropic Release of a Shocked Solid, *Phys. Rev. Lett.* **123**, 245501 (2019).
- [34] S. Plimpton, Fast parallel algorithms for short-range molecular dynamics, *J. Comput. Phys.* **117**, 1 (1995).
- [35] L. V. Zhigilei, Z. Lin, and D. S. Ivanov, Atomistic modeling of short pulse laser ablation of metals: connections between melting, spallation, and phase explosion, *J. Phys. Chem. C* **113**, 11892 (2009).
- [36] D. McGonegle, P. Heighway, M. Sliwa, C. Bolme, A. Comley, L. Dresselhaus-Marais, A. Higginbotham, A. Poole, E. McBride, B. Nagler *et al.*, Investigating off-Hugoniot states using multi-layer ring-up targets, *Sci. Rep.* **10**, 13172 (2020).
- [37] D. Perez and L. J. Lewis, Molecular-dynamics study of ablation of solids under femtosecond laser pulses, *Phys. Rev. B* **67**, 184102 (2003).
- [38] P. Lorazo, L. J. Lewis, and M. Meunier, Thermodynamic pathways to melting, ablation, and solidification in absorbing solids under pulsed laser irradiation, *Phys. Rev. B* **73**, 134108 (2006).
- [39] K. Katagiri, N. Ozaki, S. Ohmura, B. Albertazzi, Y. Hironaka, Y. Inubushi, K. Ishida, M. Koenig, K. Miyanishi, H. Nakamura, M. Nishikino, T. Okuchi, T. Sato, Y. Seto, K. Shigemori, K. Sueda, Y. Tange, T. Togashi, Y. Umeda, M. Yabashi, T. Yabuuchi, and R. Kodama, Liquid Structure of Tantalum Under Internal Negative Pressure, *Phys. Rev. Lett.* **126**, 175503 (2021).
- [40] S. Balibar and F. Caupin, Metastable liquids, *J. Phys.: Condens. Matter* **15**, S75 (2003).
- [41] L. Zheng, Q. An, Y. Xie, Z. Sun, and S. Luo, Homogeneous nucleation and growth of melt in copper, *J. Chem. Phys.* **127**, 164503 (2007).
- [42] M. E. Povarnitsyn, K. V. Khishchenko, and P. R. Levashov, Phase transitions in femtosecond laser ablation, *Appl. Surf. Sci.* **255**, 5120 (2009).
- [43] Y. Cai, H. Wu, and S. Luo, Cavitation in a metallic liquid: Homogeneous nucleation and growth of nanovoids, *J. Chem. Phys.* **140**, 214317 (2014).

- [44] A. Miotello and R. Kelly, Laser-induced phase explosion: New physical problems when a condensed phase approaches the thermodynamic critical temperature, *Appl. Phys. A* **69**, S67 (1999).
- [45] N. Bulgakova and A. Bulgakov, Pulsed laser ablation of solids: Transition from normal vaporization to phase explosion, *Appl. Phys. A* **73**, 199 (2001).
- [46] K. Sokolowski-Tinten, J. Bialkowski, A. Cavalleri, D. von der Linde, A. Oparin, J. Meyer-ter-Vehn, and S. I. Anisimov, Transient States of Matter During Short Pulse Laser Ablation, *Phys. Rev. Lett.* **81**, 224 (1998).
- [47] A. K. Upadhyay, N. A. Inogamov, B. Rethfeld, and H. M. Urbassek, Ablation by ultrashort laser pulses: Atomistic and thermodynamic analysis of the processes at the ablation threshold, *Phys. Rev. B* **78**, 045437 (2008).
- [48] M. Leitner, W. Schröder, and G. Pottlacher, Density of liquid tantalum and estimation of critical point data, *Int. J. Thermophys.* **39**, 124 (2018).
- [49] A. Dewaele, M. Mezouar, N. Guignot, and P. Loubeyre, High Melting Points of Tantalum in a Laser-Heated Diamond Anvil Cell, *Phys. Rev. Lett.* **104**, 255701 (2010).
- [50] E. N. Hahn and S. J. Fensin, Influence of defects on the shock Hugoniot of tantalum, *J. Appl. Phys.* **125**, 215902 (2019).
- [51] T. S. Sokolova, P. I. Dorogokupets, A. M. Dymshits, B. S. Danilov, and K. D. Litasov, Microsoft excel spreadsheets for calculation of P - V - T relations and thermodynamic properties from equations of state of MgO, diamond and nine metals as pressure markers in high-pressure and high-temperature experiments, *Comput. Geosci.* **94**, 162 (2016).
- [52] R. E. Cohen and O. Güseren, Thermal equation of state of tantalum, *Phys. Rev. B* **63**, 224101 (2001).
- [53] G. E. Norman, S. V. Starikov, V. V. Stegailov, I. M. Saitov, and P. A. Zhilyaev, Atomistic modeling of warm dense matter in the two-temperature state, *Contrib. Plasma Phys.* **53**, 129 (2013).
- [54] V. V. Pisarev and S. V. Starikov, Atomistic simulation of ion track formation in UO₂. *J. Phys.: Condens. Matter* **26**, 475401 (2014).
- [55] Z. Lin, L. V. Zhigilei, and V. Celli, Electron-phonon coupling and electron heat capacity of metals under conditions of strong electron-phonon nonequilibrium, *Phys. Rev. B* **77**, 075133 (2008).
- [56] B. Y. Mueller and B. Rethfeld, Relaxation dynamics in laser-excited metals under nonequilibrium conditions, *Phys. Rev. B* **87**, 035139 (2013).
- [57] N. Medvedev and I. Milov, Electron-phonon coupling in metals at high electronic temperatures, *Phys. Rev. B* **102**, 064302 (2020).
- [58] N. Hartley, P. Belancourt, D. Chapman, T. Döppner, R. Drake, D. Gericke, S. Glenzer, D. Khaghani, S. LePape, T. Ma *et al.*, Electron-ion temperature equilibration in warm dense tantalum, *High Energy Density Phys.* **14**, 1 (2015).
- [59] Y. Gan and J. Chen, Integrated continuum-atomistic modeling of nonthermal ablation of gold nanofilms by femtosecond lasers, *Appl. Phys. Lett.* **94**, 201116 (2009).
- [60] V. Schmidt, W. Husinsky, and G. Betz, Dynamics of Laser Desorption and Ablation of Metals at the Threshold on the Femtosecond Timescale, *Phys. Rev. Lett.* **85**, 3516 (2000).
- [61] J. Byskov-Nielsen, J.-M. Savolainen, M. S. Christensen, and P. Balling, Ultra-short pulse laser ablation of copper, silver and tungsten: Experimental data and two-temperature model simulations, *Appl. Phys. A* **103**, 447 (2011).
- [62] A. Pukhov, Strong field interaction of laser radiation, *Rep. Prog. Phys.* **66**, 47 (2003).
- [63] B. L. Henke, E. M. Gullikson, and J. C. Davis, X-ray interactions: Photoabsorption, scattering, transmission, and reflection at $E = 50$ – $30\,000$ eV, $Z = 1$ – 92 , *At. Data Nucl. Data Tables* **54**, 181 (1993).
- [64] S. J. Plimpton and A. P. Thompson, Computational aspects of many-body potentials, *MRS Bull.* **37**, 513 (2012).
- [65] I. Savchenko and S. Stankus, Thermal conductivity and thermal diffusivity of tantalum in the temperature range from 293 to 1800 K, *Thermophys. Aeromech.* **15**, 679 (2008).
- [66] R. K. Williams, R. S. Graves, T. L. Hebble, D. L. McElroy, and J. P. Moore, Phonon and electron components of the thermal conductivity of tantalum at intermediate temperatures, *Phys. Rev. B* **26**, 2932 (1982).
- [67] Y. V. Petrov, N. Inogamov, and K. P. Migdal, Thermal conductivity and the electron-ion heat transfer coefficient in condensed media with a strongly excited electron subsystem, *JETP Lett.* **97**, 20 (2013).
- [68] M. Bhatia, K. Solanki, A. Moitra, and M. Tschopp, Investigating damage evolution at the nanoscale: Molecular dynamics simulations of nanovoid growth in single-crystal aluminum, *Metall. and Mat. Trans. A* **44**, 617 (2013).
- [69] C. Wu and L. V. Zhigilei, Microscopic mechanisms of laser spallation and ablation of metal targets from large-scale molecular dynamics simulations, *Appl. Phys. A* **114**, 11 (2014).
- [70] J. Meza-Galvez, N. Gomez-Perez, A. Marshall, A. Coleman, K. Appel, H. Liermann, M. McMahon, Z. Konôpková, and R. McWilliams, Thermomechanical response of thickly tamped targets and diamond anvil cells under pulsed hard x-ray irradiation, *J. Appl. Phys.* **127**, 195902 (2020).
- [71] S. I. Ashitkov, P. S. Komarov, E. V. Struleva, M. B. Agranat, G. I. Kanel, and K. V. Khishchenko, The behavior of tantalum under ultrashort loads induced by femtosecond laser, *J. Phys.: Conf. Ser.* **653**, 012001 (2015).
- [72] B. Albertazzi, N. Ozaki, V. Zhakhovsky, A. Faenov, H. Habara, M. Harmand, N. Hartley, D. Ilnitsky, N. Inogamov, Y. Inubushi *et al.*, Dynamic fracture of tantalum under extreme tensile stress, *Sci. Adv.* **3**, e1602705 (2017).
- [73] M. Sliwa, D. McGonegle, C. Wehrenberg, C. A. Bolme, P. G. Heighway, A. Higginbotham, A. Lazicki, H. J. Lee, B. Nagler, H. S. Park, R. E. Rudd, M. J. Suggit, D. Swift, F. Tavella, L. Zepeda-Ruiz, B. A. Remington, and J. S. Wark, Femtosecond X-Ray Diffraction Studies of the Reversal of the Microstructural Effects of Plastic Deformation During Shock Release of Tantalum, *Phys. Rev. Lett.* **120**, 265502 (2018).
- [74] J. D. McHardy, O. B. Ball, K. Appel, C. Baehtz, M. A. Baron, R. Briggs, M. Bykov, E. Bykova, V. Cerantola, J. Chantel *et al.* (Collaboration name: EuXFEL Community Proposal #2292) Direct temperature measurement of femtosecond hard x-ray heated tantalum (2021) (unpublished).
- [75] S. V. Razorenov, G. Garkushin, G. I. Kanel, and O. N. Ignatova, The spall strength and Hugoniot elastic limit of tantalum with various grain size, *AIP Conf. Proc.* **1426**, 991 (2012).

- [76] T. Remington, E. Hahn, S. Zhao, R. Flanagan, J. Mertens, S. Sabbaghianrad, T. G. Langdon, C. Wehrenberg, B. Maddox, D. Swift *et al.*, Spall strength dependence on grain size and strain rate in tantalum, *Acta Mater.* **158**, 313 (2018).
- [77] K. K. Nanda, Liquid-drop model for the surface energy of nanoparticles, *Phys. Lett. A* **376**, 1647 (2012).
- [78] M. Nijmeijer, A. Bakker, C. Bruin, and J. Sikkenk, A molecular dynamics simulation of the Lennard-Jones liquid–vapor interface, *J. Chem. Phys.* **89**, 3789 (1988).
- [79] P. F. Paradis, T. Ishikawa, and S. Yoda, Surface tension and viscosity of liquid and undercooled tantalum measured by a containerless method, *J. Appl. Phys.* **97**, 053506 (2005).
- [80] S.-N. Luo, T. J. Ahrens, T. Çağın, A. Strachan, W. A. Goddard III, and D. C. Swift, Maximum superheating and undercooling: Systematics, molecular dynamics simulations, and dynamic experiments, *Phys. Rev. B* **68**, 134206 (2003).
- [81] S. Coleman, D. Spearot, and L. Capolungo, Virtual diffraction analysis of NI [0 1 0] symmetric tilt grain boundaries, *Modell. Simul. Mater. Sci. Eng.* **21**, 055020 (2013).
- [82] S. P. Coleman, M. M. Sichani, and D. E. Spearot, A computational algorithm to produce virtual x-ray and electron diffraction patterns from atomistic simulations, *JOM* **66**, 408 (2014).